

REPORT DOCUMENTATION PAGE			2	Form Approved OMB NO. 0704-0188	
<p>The public reporting burden for this collection of information is estimated to average 1 hour per response, including the time for reviewing instructions, searching existing data sources, gathering and maintaining the data needed, and completing and reviewing the collection of information. Send comments regarding this burden estimate or any other aspect of this collection of information, including suggestions for reducing this burden, to Washington Headquarters Services, Directorate for Information Operations and Reports, 1215 Jefferson Davis Highway, Suite 1204, Arlington VA, 22202-4302. Respondents should be aware that notwithstanding any other provision of law, no person shall be subject to any penalty for failing to comply with a collection of information if it does not display a currently valid OMB control number. PLEASE DO NOT RETURN YOUR FORM TO THE ABOVE ADDRESS.</p>					
1. REPORT DATE (DD-MM-YYYY)		2. REPORT TYPE New Reprint		3. DATES COVERED (From - To) -	
4. TITLE AND SUBTITLE A Novel Blast-mitigation Concept for Light Tactical Vehicles			5a. CONTRACT NUMBER W911NF-11-1-0518		
			5b. GRANT NUMBER		
			5c. PROGRAM ELEMENT NUMBER 611102		
6. AUTHORS M. Grujicic , B. d'Entremont , J. S. Snipes, R. Gupta			5d. PROJECT NUMBER		
			5e. TASK NUMBER		
			5f. WORK UNIT NUMBER		
7. PERFORMING ORGANIZATION NAMES AND ADDRESSES Clemson University 300 Brackett Hall Box 345702 Clemson, SC 29634 -5702			8. PERFORMING ORGANIZATION REPORT NUMBER		
9. SPONSORING/MONITORING AGENCY NAME(S) AND ADDRESS (ES) U.S. Army Research Office P.O. Box 12211 Research Triangle Park, NC 27709-2211			10. SPONSOR/MONITOR'S ACRONYM(S) ARO		
			11. SPONSOR/MONITOR'S REPORT NUMBER(S) 60050-EG.22		
12. DISTRIBUTION AVAILABILITY STATEMENT Approved for public release; distribution is unlimited.					
13. SUPPLEMENTARY NOTES The views, opinions and/or findings contained in this report are those of the author(s) and should not be construed as an official Department of the Army position, policy or decision, unless so designated by other documentation.					
14. ABSTRACT A new concept solution for improving blast survivability of the light tactical military vehicles is proposed and critically assessed using computational engineering methods and tools. The solution is inspired by the principle of operation of the rocket-engine nozzles, in general and the so called "pulse-detonation" rocket-engines, in particular. The proposed concept utilizes side vent channels attached to the V-shaped vehicle underbody whose geometry is optimized with respect to the attainment of the maximum downward thrust on the vehicle. In the course of the channel design optimization, analytical and computational analyses of supersonic flow (analogous to the one after					
15. SUBJECT TERMS Surrogate Box Structure; Blast Mitigation; Side Vent Channels; Design Optimization					
16. SECURITY CLASSIFICATION OF:		17. LIMITATION OF ABSTRACT		15. NUMBER OF PAGES	
a. REPORT UU	b. ABSTRACT UU	c. THIS PAGE UU	UU	19a. NAME OF RESPONSIBLE PERSON Mica Grujicic	
				19b. TELEPHONE NUMBER 864-656-5639	

Report Title

A Novel Blast-mitigation Concept for Light Tactical Vehicles

ABSTRACT

A new concept solution for improving blast survivability of the light tactical military vehicles is proposed and critically assessed using computational engineering methods and tools. The solution is inspired by the principle of operation of the rocket-engine nozzles, in general and the so called “pulse-detonation” rocket-engines, in particular. The proposed concept utilizes side vent channels attached to the V-shaped vehicle underbody whose geometry is optimized with respect to the attainment of the maximum downward thrust on the vehicle. In the course of the channel design optimization, analytical and computational analyses of supersonic flow (analogous to the one often used in the case of the pulse detonation engine) are employed. The preliminary results obtained reveal the beneficial effects of the side channels in reducing the blast momentum, although the extent of these effects is relatively small (2-4%).

REPORT DOCUMENTATION PAGE (SF298)
(Continuation Sheet)

Continuation for Block 13

ARO Report Number 60050.22-EG
A Novel Blast-mitigation Concept for Light Tactic..

Block 13: Supplementary Note

© 2013 . Published in ARL Technical Report ARL-TR-6735, Vol. Ed. 0 (2013), (Ed.). DoD Components reserve a royalty-free, nonexclusive and irrevocable right to reproduce, publish, or otherwise use the work for Federal purposes, and to authorize others to do so (DODGARS §32.36). The views, opinions and/or findings contained in this report are those of the author(s) and should not be construed as an official Department of the Army position, policy or decision, unless so designated by other documentation.

Approved for public release; distribution is unlimited.

A NOVEL BLAST-MITIGATION CONCEPT FOR LIGHT TACTICAL VEHICLES

M. Grujicic, B. d'Entremont, J. S. Snipes
Department of Mechanical Engineering
Clemson University, Clemson SC 29634

R. Gupta
Army Research Laboratory
Blast Protection Branch, Protection Division
Aberdeen, Proving Ground, MD 21005-5066

Correspondence to: ¹

Mica Grujicic, 241 Engineering Innovation Building, Clemson University, Clemson, SC 29634-0921;
Phone: (864) 656-5639, Fax: (864) 656-4435, E-mail: gmica@clemson.edu

ABSTRACT

A new concept solution for improving blast survivability of the light tactical military vehicles is proposed and critically assessed using computational engineering methods and tools. The solution is inspired by the principle of operation of the rocket-engine nozzles, in general and the so called “*pulse-detonation*” rocket-engines, in particular. The proposed concept utilizes side vent channels attached to the V-shaped vehicle underbody whose geometry is optimized with respect to the attainment of the maximum downward thrust on the vehicle. In the course of the channel design optimization, analytical and computational analyses of supersonic flow (analogous to the one often used in the case of the pulse detonation engine) are employed. The preliminary results obtained reveal the beneficial effects of the side channels in reducing the blast momentum, although the extent of these effects is relatively small (2-4%).

I. INTRODUCTION

In the present work, a new concept solution for improving blast-survivability of the light tactical military vehicles is proposed and investigated using computational

Keywords: Surrogate Box Structure; Blast Mitigation; Side Vent Channels; Design Optimization

engineering methods and tools. The solution is inspired by the principle of operation of the rocket-engine nozzles, in general and the so called “*pulse-detonation*” rocket-engines, in particular [1]. Hence, the main topics to be overviewed in this introductory section of the present manuscript include: (a) main limitations of the (light) tactical vehicles currently in use; (b) principle of operation of a rocket-engine nozzle; and (c) the principles of operation of pulse-detonation rocket-engines.

Limitations of the Current Tactical Vehicles: The HMMWV (High Mobility Multipurpose Wheeled Vehicle) is the prototypical light tactical vehicle used by the US military. This vehicle was designed/developed during the cold war and, not surprisingly, has been found lacking the necessary blast and ballistic resistance in the ongoing asymmetric warfare, in which the distinction between front line combat and transportation convoys has been severely blurred. Thus, in conflicts in Iraq and Afghanistan, HMMWVs have mostly been replaced by larger, heavier MRAP (Mine Resistant Ambush Protected) vehicles, which have been specifically designed for resistance to IEDs (Improvised Explosive Devices) blast.

However, the added mass which plays a key role in the superior IED survivability of the MRAP, also negatively affects other performance aspects of this vehicle such as: (a) tactical utility/mobility is severely compromised relative to that of the HMMWV; (b) diminished maneuverability on narrow city streets; (c) poor fuel economy; (d) its weight exceeds the payload capacity of the CH-47 Chinook helicopter severely affecting its transportability; and (e) its weight exceeds the load carrying capacity of 72% of the world’s bridges [2] seriously hampering its deployment.

Principle of Operation of a Rocket-Engine Nozzle: In the subsonic flow regime, a fluid can be accelerated by passing it through a converging nozzle. In this case, to ensure constancy of the mass flow rate, the fluid velocity at the nozzle exit must be higher than that at the nozzle inlet. The force required to accelerate the fluid in the subsonic regime is derived solely from the higher upstream pressure. The effect of higher upstream pressure is propagated through the advancing fluid at the speed of sound. Hence, once the fluid at the nozzle exit reaches the sonic velocity, further increase in the fluid upstream pressure will not cause an additional increase in the fluid exit velocity. Simply

stated, since the fluid at the nozzle exit flows at the sonic speed, the information regarding the increased upstream pressure never reaches the exiting fluid. A converging nozzle in which the fluid exit velocity is the sonic velocity is referred to as being in the “*choked-flow*” condition.

The analysis presented above shows that the fluid cannot be accelerated into the supersonic regime by simply pushing-off against the upstream fluid. Consequently, to achieve the supersonic flow condition, the fluid should be provided with a forward facing solid surface upon which the flow can exert a force. This is the reason that a typical rocket-engine nozzle contains not only a converging but also a subsequent diverging section. In this type of nozzle design, the converging section accelerates the fluid from subsonic to sonic velocity while the diverging section accelerates the fluid from a sonic to supersonic velocity. The converging-diverging rocket-engine nozzle design described here is typically referred to as the “*de Laval*” nozzle.

As the fluid is being accelerated into the supersonic regime, it exerts a force (in the direction opposite to the flow) on the walls of the diverging sections of the nozzle. It is this force that provides a thrust/propulsion to the rocket. To maximize the amount of thrust for a given level of the fluid pressure at the nozzle throat (transition between the converging and diverging sections of the nozzle), the exit velocity of the fluid (from the diverging section of the nozzle) must be maximized while ensuring that the exiting fluid is at the ambient pressure condition. This condition is generally referred to as the “*ideally-expanded*” fluid flow. If this condition is not attained, the fluid flow could be either “*under-expanded*” (the fluid exit pressure is higher than the ambient pressure) or “*over-expanded*” (the fluid exit pressure is lower than the ambient pressure). Both of these conditions are undesirable since they yield a lower value of the propulsion thrust. Specifically, in the case of the under-expanded flow, the potential of the expanding fluid to push-off the walls of the diverging section of the nozzle has been under-utilized. On the other hand, in the case of the over-expanded flow, a stationary shock is formed at the nozzle exit which reduces effectively the momentum of the fluid exiting the nozzle.

To attain the ideally-expanded flow condition for the given values of the fluid pressure at the nozzle throat and the ambient pressure, one typically carries out a one dimensional steady (time-invariant) isentropic (no thermal conduction or energy

exchange) fluid-expansion analysis. The outcome of this analysis is the optimal nozzle exit-to-throat area ratio which provides the maximum propulsion thrust. Below, an example of this analysis which utilizes the mass and energy (but not linear momentum) conservation equations is provided. It should be noted that the identical final results could be obtained using an analogous analysis which combines the mass and the linear momentum conservation equations.

For a calorically perfect (i.e. temperature-invariant specific heat), inviscid (i.e. zero viscosity), ideal gas undergoing adiabatic, one-dimensional expansion, the conservation of energy requires:

$$C_p T_1 + \frac{V_1^2}{2} = C_p T_2 + \frac{V_2^2}{2} \quad (1)$$

where C_p denotes constant-pressure specific heat, T the absolute temperature, V the fluid velocity and subscripts 1 and 2 refer to the nozzle inlet (more precisely the throat) and the exit conditions. It should be noted that the two terms on each side of Eq. (1), denote respectively the mass-based thermal and kinetic-energy-density components. Eq. (1) can be rearranged as:

$$\frac{T_2}{T_1} = \frac{1 + V_1^2 / (2C_p T_1)}{1 + V_2^2 / (2C_p T_2)} \quad (2)$$

Using the definition of the Mach number $M=V/C_s$, where $C_s (= \sqrt{\gamma RT})$, γ is the constant-pressure to the constant-volume specific-heat ratio, R is the gas-specific gas constant) denotes the speed of sound in the fluid, one can show that

$V^2 / (2C_p T) = \frac{1}{2}(\gamma - 1)M^2$ and, in turn, rewrite Eq. (2) as:

$$\frac{T_2}{T_1} = \frac{1 + \frac{1}{2}(\gamma - 1)M_1^2}{1 + \frac{1}{2}(\gamma - 1)M_2^2} \quad (3)$$

Using the functional relationship for a P - T isentrope, where P denotes pressure,

$PT^\gamma = \text{Const.}$, Eq. (3) could be recast as:

$$\frac{P_2}{P_1} = \left(\frac{T_2}{T_1} \right)^{\frac{\gamma}{\gamma-1}} = \left(\frac{1 + \frac{1}{2}(\gamma-1)M_1^2}{1 + \frac{1}{2}(\gamma-1)M_2^2} \right)^{\frac{\gamma}{\gamma-1}} \quad (4)$$

or

$$M_2 = \sqrt{\left(\frac{2}{\gamma-1} + M_1^2 \right) \left(\frac{P_1}{P_2} \right)^{\frac{\gamma-1}{\gamma}} - \frac{2}{\gamma-1}} \quad (5)$$

For the given values of the nozzle throat fluid pressure P_1 , velocity V_1 and temperature T_1 and the nozzle exit fluid pressure P_2 (= ambient pressure), Eq. (5) enables the calculation of the fluid exit Mach number associated with the ideally-expanded flow. However, one would also like to know the nozzle exit-to-throat area ratio which should be used to attain this condition. This can be done through the use of the mass conservation equation which can be defined as:

$$A_1 \rho_1 V_1 = A_2 \rho_2 V_2 \quad (6)$$

or

$$\frac{A_2}{A_1} = \left(\frac{V_1}{V_2} \right) \left(\frac{\rho_1}{\rho_2} \right) \quad (7)$$

where ρ represents mass density and A the nozzle cross-sectional area. Using the functional relationship for a P - ρ isentrope, $\frac{P}{\rho^\gamma} = Const.$, the aforementioned P-T

isentropic relation and the Mach number definition, Eq. (7) can be rewritten as:

$$\frac{A_2}{A_1} = \left(\frac{P_1}{P_2} \right)^{\frac{1+\gamma}{2\gamma}} \left(\frac{M_1}{M_2} \right) \quad (8)$$

Eq. (8) shows that once the state of the fluid (including its velocity) at the nozzle throat and the ambient pressure are known, one can compute the optimal nozzle exit to throat area ratio (associated with the “*ideally-expanded*” fluid-flow condition) which yields the maximum (backward) thrust on the diverging section of the nozzle.

An example of the results obtained in this type of analysis is depicted in Figure 1 for the case of air with the following air-material parameters, the nozzle-throat material states and the ambient-air pressure: $\gamma=1.4$, $P_I=3\text{MPa}$, $\rho_I= 4\text{kg/m}^3$, $V_I=900\text{m/s}$ and $P_2=101.3\text{kPa}$. The optimal nozzle cross-section-area ratio is denoted by a solid circle in this figure. It should be noted that the functional relationship between exit Mach number and the area ratio, Eqs. (5) and (8), are valid only under the ideal expansion conditions i.e. when the nozzle exit pressure is equal to the ambient pressure. When this condition is not met, the exit momentum of the fluid is altered/lowered by the presence of a stationary decompression simple wave at the nozzle exit (in the case of an under-expanded flow) or by the presence of a stationary (compression) shock (in the case of an over-expanded flow). While an analysis involving the contribution of these waves/shocks is beyond the scope of the present work, the exit momentum predictions based on the inclusion of the shock effects is also shown in Figure 1. Examination of the results displayed in Figure 1 shows that the optimum nozzle cross-sectional area ratio is ca. 5.06.

To calculate the associated thrust force, F_{thrust} , the linear momentum conservation equation should be employed as:

$$A_2\rho_2V_2^2 - A_1\rho_1V_1^2 = (P_1A_1 - P_2A_2) + F_{thrust} \quad (9)$$

The net quantity on each side of Eq. (9) represents the total force acting on the fluid within the nozzle, F_{Fluid} . By combining Eqs. (6) and (9) with the Mach number definition and the P - ρ isentrope, the fluid force per unit nozzle inlet cross-sectional area can be defined as:

$$\frac{F_{Fluid}}{A_1} = \rho_1V_1 \left(M_2 \sqrt{\gamma \frac{P_2}{\rho_1 \left(\frac{P_2}{P_1}\right)^\gamma}} - V_1 \right) \quad (10)$$

For the aforementioned air inlet states and the normal ambient pressure, the fluid force per unit nozzle inlet cross-sectional area corresponding to the ideal nozzle

cross-sectional area ratio was found to be ca. 4.02 MN/m^2 . The calculation of the thrust force requires the knowledge of the nozzle inlet and outlet cross-sectional areas.

Principle of Operation of the Pulse-detonation Rocket-Engine: The rocket-engine nozzle design analysis presented above deals with a steady, continuous flow and assumes the existence of sonic flow at the nozzle throat. These flow conditions are generally not encountered in the case of a mine-detonation event. That is, the flow is in the transient (not steady) state, it involves a single pulse (rather than being continuous) and the gaseous detonation products, from the onset, are already in the supersonic flow regime. Thus, a natural question arises as to whether the aforementioned analysis is adequate or even relevant to the problem of blast-mitigation system design. To address this question, it is first recognized that there are some similarities between the so-called “*pulse detonation*” engine and a prototypical mine detonation event. These similarities pertain to the characteristic times (several hundred microseconds) of the associated blast events and in the fact that the fluids in question (detonation by-products and fuel/oxidizer mixture combustion products) are, from the onset, in the supersonic flow regime. Consequently, a brief overview of the principles of operation of a pulse-detonation engine is given in this section.

The pulse-detonation engine (the subject of active ongoing research and development) is an intermittent combustion engine and is a variant of the pulse-jet engine, a simple engine with no moving parts. The latter engine was famously employed in the German V-1 “*buzz bomb*” during World War II. The main difference between the pulse-detonation engine and most of the current rocket engines (including pulse-jet engines) is that in the former case fuel-oxidizer combustion (detonation) takes place at a supersonic speed while in the latter case the combustion rate is subsonic (i.e. it is in the deflagration regime). As will be discussed below, this difference results in an improved thermodynamic efficiency of the pulse detonation engine.

A pulse-detonation engine, Figure 2, typically consists of a combustion/detonation chamber equipped with a fuel-oxidizer inlet valve, a thrust wall (at the front) and a diverging exhaust nozzle (at the back). A single engine cycle begins with air/oxidizer mixture entering through the inlet valve. The inlet valve is then closed

and fuel is injected to create a detonatable mixture. The mixture is ignited from the front end, resulting in a detonation wave which travels rearward and exits through the exhaust nozzle, resulting in a short term, high-velocity outflow of combustion products. This process creates under-pressure in the front portion of the combustion chamber and provides the conditions necessary for the intake of the fuel-oxidizer mixture for the next cycle. Due to the isentropic expansion of the combustion products exiting the exhaust nozzle, intermittent thrust is generated in the forward direction.

As discussed earlier, in contrast to most rocket engines, in general, and pulse-jet engines in particular, which rely upon the rapid deflagration of the fuel-oxidizer mixture, pulse-detonation engines utilize detonation of the same mixture. In other words, while in the case of a pulse-jet engine the combustion front advances relatively slowly (since the rate of combustion is limited by heat conduction/convection), in the case of the pulse-detonation engine the combustion front advances at a supersonic velocity (since the combustion process is initiated by the arrival of the shock/detonation wave). This difference in the rate of combustion gives rise to several important advantages for the pulse-detonation engine such as: (a) improved thermodynamic efficiency due to the fact that combustion takes place under constant-volume rather than constant-pressure conditions [4]. Simply stated, in the case of pulse-jet engines, the combustion-induced shock wave expels a considerable amount of unburned fuel-oxidizer mixture through the nozzle exit (while maintaining fairly constant pressure level within the combustion chamber). In the case of the pulse-detonation engines on the other hand, effectively no expulsion of the unburned fuel/oxidizer mixture takes place; (b) as a consequence of (a), significant improvements are attained in the specific impulse generated by the engine; and (c) due to a very short cycle time (several 100's of microseconds), the pulse-detonation engines run, for all practical purposes, continuously, which results in greatly reduced vibrations.

When designing a rocket engine, a substantial effort is invested in optimizing the shape of the exhaust nozzle in order to maximize the amount of forward propulsion thrust. It should be noted that, due to the intermittent character of the combustion process, the nozzle-design optimization in the case of pulse-detonation engines is more challenging than in the case of the conventional (continuous-flow) rocket engines.

Specifically, in the case of the continuous-flow engines, variations in the combustion chamber pressure are relatively small and, hence, the exhaust nozzle design is optimized to a relatively narrow range of nozzle inlet-to-outlet pressure ratios. In sharp contrast, in the case of pulse-detonation engines, the pressure ratio across the nozzle peaks with the arrival of the detonation wave at the nozzle inlet and then diminishes as the combustion products exit the combustion chamber through the exhaust nozzle. This process is typically referred to as “*blowdown*” [3]. It is this variability of the pressure ratio across the nozzle which makes its design and optimization a complicated process.

The problem of the optimal design of the exhaust nozzle for the pulse detonation engine has been recently addressed by Owens and Hanson [3] who studied the effect of exhaust nozzle shapes (a straight tube, a converging-diverging nozzle, and a diverging nozzle) on the specific impulse delivered. They employed a numerical, quasi-one-dimensional analysis in which kinetics of the combustion elementary chemical reactions is combined with the mass, momentum and energy conservation equations in order to determine the optimal nozzle shape and the area ratios for maximum propulsion thrust. The computational results were subsequently validated in a companion experimental investigation. Their investigation yielded two important findings: (a) among the nozzle shapes tested, the diverging nozzle produced the maximum propulsion thrust; and (b) for each of the three nozzle shapes tested, the optimum area ratio was found to be quite close to the one that could be obtained through the use of a steady isentropic expansion-flow analysis (of the type discussed in the previous section) in which the (constant) pressure ratio across the nozzle is replaced with the time-average of the corresponding variable pressure ratio over the duration of a single combustion cycle. The latter finding is quite interesting since it suggests that, despite the fact that many of the conditions associated with the steady isentropic-expansion analysis are not met in the course of a pulse-detonation engine cycle, this analysis may still be relevant when carrying out design optimization of a pulse-detonation engine exhaust nozzle.

Objective: The conventional V-hull blast-mitigation solution is depicted schematically in Figure 3(a). In this case, the blast-mitigation performance increases with an increase in

the V-hull steepness. However, constraints associated with vehicle ground clearance and height limit the maximum allowable V-hull steepness. A truncated V-hull design is depicted in Figure 3(b). In this case, the blast-mitigation performance is enhanced relative to that offered by the design depicted in Figure 3(a), since the benefits (decreased blast impulse) offered by the increased steepness of the V-hull outweigh the penalty (i.e. increased blast impulse) incurred due to the small flat section.

In the present work, an attempt is made to develop a concept-level solution for an alternative blast-mitigation system to the ones displayed in Figures 3(a)–(b). The basic requirement for the new concept solution is to surpass the blast-mitigation performance of the V-hull solution, while not intruding into the interior cabin space or compromising structural durability of the vehicle. As will be discussed in the next section, this alternative solution utilizes side-vent channels attached to the V-shaped vehicle underbody. The main purpose of the channels is to direct flow upward at maximum velocity and, thus, maximize the downward thrust on the vehicle. Channel shaping was conducted by combining a conventional design-optimization methodology with the analytical and computational analyses of supersonic flow (analogous to the ones overviewed above in the case of the pulse-detonation engine).

Organization: In Section II, a brief description is provided of the proposed blast-mitigation concept. The utility of the continuous-steady isentropic-expansion analysis in identifying the optimal area-ratio across the channels/tubes which maximizes the downward thrust is addressed in Section III. A simplified two-dimensional mine-blast computational analysis is carried out in Section IV. Section V contains a more refined three-dimensional analysis of the same problem. The main conclusions resulting from the present work are listed in Section VI.

II. CONCEPT DESCRIPTION

In this section, a brief description is provided of the new blast-mitigation concept proposed in the present work. It is hoped that the proposed concept can help with the development of lighter, high-mobility/maneuverability, fuel-efficient, transportable and deployable light tactical vehicles with improved mine/IED survivability. To prevent

potential misuse, of the ideas proposed and the results obtained in the present work, the term “*vehicle*” will be replaced with the term “*surrogate box structure*” (SBS).

The proposed concept is depicted schematically in Figure 4 and involves the use of tubes/channels (of the appropriate cross-sectional shape and wall thickness) attached to the underside of a V-shaped hull and open at both ends. The bottom end of each tube is cut parallel to the ground (to promote inflow of the detonation by-products and soil ejecta, and to prevent structural collapse (crushing) of the tube inlet under blast loads) and flush with the V-hull bottom. The channels/tubes are intended to function as exhaust nozzles in the case of the pulse-detonation engine and, thus, provide a downward thrust to the vehicle. This downward thrust is expected to offset some of the blast-induced impulse delivered to the vehicle and thus lower the possibility for the vehicle lift-off from the ground. The secondary role of the channels/tubes is to enable the venting of the gaseous detonation products, soil ejecta and mine-casing fragments. It should be noted that the blast venting effect offered by the side-vent channels complements the reduced blast-impulse effect offered by the conventional V-shaped vehicle hulls.

It should be noted that the concept proposed here builds on the similarities between a mine-detonation event and a pulse-detonation-engine combustion cycle. In particular, explosion of a mine is a short duration event which creates shock waves in air and the impingement of these waves on to the target structure causes a momentum transfer. Similar events occur in the course of a pulse-detonation-engine cycle except that the shock waves propagate through the fuel-oxidizer mixture and give rise to mixture combustion.

The geometry of the channels/tubes is optimized in order to maximize the downward thrust resulting from the supersonic expansion of the gaseous detonation products. Specific design parameters include variation of tube cross-sectional area along its length and the orientation of the tube top-end cut.

In the channel/tube design-optimization analysis both the analytical, steady isentropic-expansion analysis (with the stagnation pressure equal to the time-averaged detonation product pressure at the channel/tube inlet) and a transient numerical analysis are employed. The analytical analysis is identical to the one reviewed in the

previous section while the numerical analysis is described in greater detail in the next section.

III. CONTINUOUS-STEADY vs. PULSED-TRANSIENT FLOW ANALYSES

The two main objectives of the work presented in this section are: (a) to establish the capability of the employed computational methods and tools for reproducing the basic results yielded by the continuous-steady isentropic-expansion analysis; and (b) to address the question of utility of the continuous-steady isentropic-expansion analysis in identifying the optimal area-ratio across the channels/tubes which maximizes the downward thrust on the SBS (under pulsed-transient flow, i.e. blast-loading conditions). The steady isentropic analysis was presented in Section I, where it was shown that the knowledge of the fluid inlet states and properties as well as the ambient pressure is required in order to compute the optimum channel-area ratio along with the exit Mach number and the thrust force per unit inlet cross-sectional area. Details of the numerical pulsed-transient flow analysis are presented below. It should be noted that, in the present analysis, the presence of soil within the fluid passing through the channel is not accounted for, either explicitly or implicitly. Thus, the analysis may be deemed more relevant to the case of ground-laid explosives and less relevant to the buried-mine detonation cases.

III.1 STEADY/TRANSIENT FLOW COMPUTATIONAL PROCEDURE

Computational Domain: A typical computational domain used in the present analysis is depicted in Figure 5. It contains a circular cross-section channel in which the end segments have constant (but different) radii, and in the middle section the radius transitions linearly along the channel length. To take advantage of the symmetry of the model, only one-quarter of the channel is explicitly analyzed. Typically, the computational domain is meshed using ca. 10000 hexahedron first-order reduced-integration Eulerian elements.

Computational Analysis Type: The fluid flow through the channel is analyzed using a thermo-mechanical purely Eulerian formulation within which the mesh is fixed in space

while the fluid is allowed to flow through it. The flow is assumed to be of a laminar character since the finite-element program used, ABAQUS/Explicit [5] does not contain any turbulence models. While it is beyond the scope of the present work to provide quantitative assessment of the turbulence effects, these effects are expected not to have a first-order influence on the results reported later in this section. This conjecture is based on the fact that the flow fields in the present case are dominated by the strong, unidirectional/axial component of the field variables.

Initial Conditions: The computational domain is initially filled with different material states, depending on the main objective of the computational analysis. That is, in the analysis in which the main objective was validation of the employed numerical methods and tools, the initial material state is set equal to that predicted by the continuous-steady isentropic-expansion analysis for the inlet pressure of 3 MPa, inlet fluid density of 4 kg/m^3 , inlet particle velocity of 900 m/s and the ambient value of the outlet pressure. On the other hand, in the computational investigations in which the main objective was establishment of the utility of the continuous-steady isentropic-expansion analysis, the following material states were assigned: (a) the initial straight section of the channel is assigned the initial pressure, density, temperature and particle velocity consistent with the von Neumann point source approach [19], explosive energy $E_0=10 \text{ MJ}$, and the channel-inlet stand-off distance of 1 m [6–9]. Within the point-source approach, the explosive charge is shrunken to a point and, under an “*ideal-explosion assumption*” (i.e. under a condition that the ambient pressure is so small in comparison to the detonation pressure that it could be neglected), the similarity property of the point-source solution can be taken advantage of in order to compute spatial distribution of the material states in the vicinity of the point-source. Clearly, due to a rapid decrease in the detonation pressure with time, the ideal-explosion assumption is valid only over a very short post-detonation time. A summary of the point-source results generated in the present work, following the procedure described in Ref. [19], is given in Figures 6(a)–(d). In these figures, a standoff distance (relative to the detonation site) normalized by the radial position (also relative to the detonation site) of the blast-wave front is plotted along the x -axis. As far as the y -axis is concerned,

it displays, in each case, the appropriate material-state variable normalized by its value at the blast-wave front. The material-state variables depicted in Figures 6(a)–(d) are respectively: mass density, particle velocity, static pressure and absolute temperature. The aforementioned similarity property of the point-source solution simply states that the plots shown in Figures 6(a)–(d) are time-invariant, as long as the ideal-explosion condition is satisfied; and (b) the remainder of the channel is filled with quiescent, atmospheric-pressure air.

Boundary Conditions: To account for the two-orthogonal-plane symmetry of the computational model, the appropriate symmetry (i.e., zero normal velocity) boundary conditions are applied along the flat faces (parallel to the symmetry planes) of the quarter model shown in Figure 5. Zero normal velocity conditions are applied also along the curved face of the channel. The use of the last boundary condition indicates that the channel walls are treated as rigid and immobile. In our future work, channel walls will be treated as deformable and, hence, an appropriate Fluid-Structure Interaction (FSI) contact algorithm will be used in place of the boundary condition in question. Also, to comply with one of the basic simplifications within the theory of gas dynamics, zero-friction boundary conditions are enabled along the curved face of the computational domain. The pressure at the channel exit is maintained at the ambient pressure level (101 kPa) while the inlet pressure is: (a) maintained at 3 MPa, in the cases in which the main objective was validation of the employed computational methods and tools; and (b) varied in accordance with the point-source decaying-shock solution mentioned in the initial-condition section, in the computational investigations in which the main objective was establishment of the utility of the continuous-steady isentropic expansion analysis.

Fluid/Channel-Wall Interactions: While the channel walls are not explicitly modeled, the nature of the velocity boundary conditions along the curved face of the quarter-model described above implies that the channel walls are modeled implicitly as being rigid with zero-friction conditions along the fluid channel-wall contact surfaces. It should be noted that since the channel-wall was not modeled explicitly, the thrust force exerted on this wall cannot be directly calculated. Rather, the associated force acting on the fluid

within the channel could be assessed from the difference in the exiting and the incoming momentum of the fluid, Eq. (9). In addition, since no FSI effects are included at the air/channel-wall interface (i.e. the wall is not allowed to expand outward and relieve some of the pressure acting on it), the downward thrust effects (reported later in this section) are expected to be somewhat overestimated.

Material Model: As mentioned earlier, the Eulerian domain was filled with air. Air was modeled as an ideal gas and, consequently, its equation of state was defined by the ideal-gas gamma-law relation as [10]:

$$P = (\gamma - 1)\rho E \quad (11)$$

where $E (=C_v T)$ is the mass-based internal energy density and C_v is the constant volume specific heat. For Eq. (11) to yield the standard atmospheric pressure of 101.3kPa and the standard air density of 1.19kg/m³ at the standard temperature of 293K with $\gamma=1.4$, the corresponding mass based internal energy density has to be set to 211.5kJ/kg.

Since air is a gaseous material, it has zero shear stiffness. However, shear stresses can be developed as a result of a gradient in the flow velocity. A provision is made for viscous shear stresses in the present work while assuming a Newtonian fluid-like behavior, i.e. the shear stress scales linearly with the velocity gradient with the proportionality constant, the viscosity, being set at $1.78 \cdot 10^{-5}$ Pa·s.

Computational Algorithm: The governing mass, linear momentum and energy conservation and heat conduction equations are solved within ABAQUS/Explicit with a second-order accurate, conditionally stable, explicit finite element algorithm. Within each time increment, the solution procedure for the aforementioned governing equations involves two distinct steps: (i) the Lagrangian step within which the computational domain is temporarily treated as being of a Lagrangian-type (i.e. nodes and elements are attached to and move/deform with the material); and (ii) the “*remap*” step within which the distorted mesh is mapped onto the original Eulerian mesh and the accompanying material transport is computed and used to update the Eulerian-material states and inter-material boundaries.

Computational Accuracy, Stability and Cost: A standard mesh sensitivity analysis was carried out (the results not shown for brevity) in order to ensure that the results obtained are accurate, i.e. insensitive to the size of the elements used.

Due to the conditionally-stable nature of the explicit finite element analysis used, the maximum time increment during each computational step had to be lower than the attendant stable time increment. A typical 25ms computational analysis followed by a detailed post-processing data-reduction analysis required on average 30 minutes of (wall-clock) time on a 12 core, 3.0GHz machine with 16GB of memory.

III.2 RESULTS AND DISCUSSION

Continuous-Steady Flow Analysis: To assess the accuracy of the Eulerian finite element analysis carried out in the present work using ABAQUS/Explicit [5], an attempt was made to reproduce the key results yielded by the continuous-steady isentropic analysis for the material-state boundary conditions specified in the previous section. Examples of the typical results obtained in this portion of the work are displayed in Figures 7(a)–(c).

Figure 7(a) shows the temporal evolution of the fluid force per inlet unit area (solid curve). This force is obtained by dividing the total fluid force (calculated as a sum, over all the Eulerian nodes, of the product of mass allotted to each node and the corresponding nodal (axial) acceleration) by the channel inlet area. In the same figure, the fluid force per unit inlet area predicted by the analytical steady isentropic-expansion analysis is denoted with a dashed horizontal line. Examination of the results displayed in Figure 7(a) shows that the numerically predicted steady force (per unit inlet area) exerted on the fluid in the axial direction is smaller (by about 10%) than its analytical isentropic-expansion counterpart.

To provide a rationale for the aforementioned discrepancy between the numerical and the analytical results, flow fields through the Eulerian domain are examined and compared with their analytical counterparts. An example of this comparison is shown in Figures 7(b)–(c). In these figures, fluid (axial and resultant) velocities are plotted for the analytical case, Figure 7(b), and for the numerical case, Figure 7(c). The axial component of the velocity was represented using a contour plot,

while arrows are used to denote (the magnitude and the orientation of) the resultant velocity. It is seen that the analytical solution assumes that the flow is entirely in the axial direction while the numerical results show that the flow contains a significant radial component (in the diverging section of the computational domain). It should be noted that the observed differences between the analytical and the numerical solutions seen in Figures 7(b) and (c) do not invalidate the computational procedure used but simply indicate that the flow field is not entirely axial, as postulated in the analytical steady isentropic-expansion analysis.

Pulsed-Transient Flow Analysis: As mentioned above, the main purpose of this portion of the work was to establish if the steady isentropic-expansion analysis can be used, in place of a pulsed-transient flow analysis, to determine the optimum area ratio which maximizes the downward thrust on the SBS. An example of the results obtained in this portion of the work is displayed in Figure 8, in which the effect of the varying channel cross-sectional-area ratio on the (axial) impulse exerted on the fluid within the channel is displayed. A single black-color filled square symbol is used, in the same figure, to denote the optimal area ratio and the associated impulse per unit area as predicted by the analytical steady isentropic-expansion analysis (based on the time-averaged inlet pressure and the same blast-loading time). Examination of the results displayed in Figure 8 shows that the optimal area ratio predicted by the present numerical procedure (ca. 3.24) is approximately 36% smaller than its analytical counterpart (ca. 5.06). In addition, the numerically predicted maximum value of the impulse per unit area is substantially lower than its analytical counterpart. These differences between the numerical and the analytical results are quite large and are in sharp contrast with the findings of Owens and Hansen [3] and suggest that the use of the analytical isentropic-expansion analysis in predicting the optimum area ratio of a channel may not be very reliable under blast-loading conditions.

IV. TWO-DIMENSIONAL MINE-BLAST FLUID-STRUCTURE INTERACTION ANALYSIS

In the previous section, a purely Eulerian computational analysis is carried out to study the detonation products flow through a prototypical side channel. In that case,

detonation of a mine buried in soil/sand and the accompanying expulsion of the gaseous detonation products, soil ejecta and mine-casing fragments was not explicitly modeled. Instead, the mine blast was assumed to merely generate high-pressure, high-density supersonic velocity gaseous detonation products which are vented through the side channels. Clearly, such an analysis is oversimplified and one might question its utility relative to assessing the blast-mitigation potential of a new concept. To overcome these shortcomings of the aforementioned analysis, in this section, a combined Eulerian/Lagrangian finite element analysis of a prototypical buried-mine detonation event is carried out. In this analysis, mine-detonation products, soil as well as the target structure equipped with the blast-mitigation side channels are all modeled explicitly. Since the computational cost of a fully three-dimensional investigation is quite high and not fully justified at the concept-validation stage analyzed in the present work, a simpler, computationally more efficient two-dimensional analysis is first utilized. A more complete three-dimensional analysis of the same problem will be presented in the next section.

IV.1 COMPUTATIONAL PROCEDURE

A brief description regarding the computational model and the numerical procedure used in this portion of the work is described below.

Computational Domain: The computational domain used consists of two separate sub-domains, one of an Eulerian-type and the other of a Lagrangian-type, Figure 9. The Eulerian sub-domain (used to model sand/soil, mine/detonation products and the ambient air) is of a parallelepiped shape. This sub-domain is typically discretized using hexahedral first-order reduced-integration Eulerian elements. Due to the aforementioned two-dimensional nature of the model, the mesh shown in Figure 9 extends only one element in the direction normal to the figure. Also, it should be noted that due to the inherent symmetry of the problem, only one-half of the computational model is explicitly analyzed.

As far as the Lagrangian sub-domain is concerned, it contains three hexahedral first-order reduced-integration Lagrangian elements. One of the elements represents the cabin combined with the V-shaped hull. The other two elements define the inclined

and the vertical segments of the side-channel outer wall. The three Lagrangian elements are rigidized and grouped into a single rigid body. During the channel-geometry optimization, both the width of the channel and the exit cross-sectional area are varied. The width of the channel was varied by displacing the inclined and the vertical segments in the horizontal direction. The exit cross-sectional area is varied by changing the length of the inclined segment at its upper end.

Computational-Analysis Type: The mine blast event is analyzed computationally using a Combined Eulerian-Lagrangian and a fully-coupled thermo-mechanical finite-element algorithm. Within the Lagrangian subdomain of the model, the mesh is attached to the underlying material and moves and deforms with it, while within the Eulerian subdomain, the mesh is stationary and different (Eulerian) materials are allowed to move through it. Heat dissipation associated with plastic deformation (of soil) is treated as a heat source in the governing thermal equation. On the other hand, the effect of temperature on the mechanical response of the attendant materials is taken into account through the use of temperature-dependent material properties.

Initial Conditions: The Eulerian subdomain is initially filled with soil/sand, mine and the ambient air (by prescribing the corresponding material volume fractions), all at their respective standard state conditions. The Lagrangian subdomain is assumed to be initially stationary.

Boundary Conditions: To account for the planar symmetry of the problem, the appropriate zero-normal-velocity boundary conditions are applied along the symmetry plane. The Eulerian boundaries associated with the soil are given non-reflecting outflow boundary conditions to prevent unphysical reflection of the shock at these boundaries. On the other hand, the Eulerian boundaries associated with the air are given no-inflow and free-outflow boundary conditions. Instead of fixing it fully in space, the Lagrangian portion of the model is allowed to move, but only in the vertical direction. This approach enabled capturing of the aforementioned FSI effects.

Euler-Lagrange Contact Conditions: Since the Eulerian and Lagrangian domains do not possess conformal meshes, the contact interfaces between the two could not be defined

using mesh-based surfaces. Instead, contact interfaces between the Lagrangian and the Eulerian subdomains are determined using the so-called “*immersed boundary method*” [5] which identifies, during each computational time increment, the boundary of the Eulerian subdomain region which is occupied by the Lagrangian subdomain. Eulerian-Lagrangian contact constraints are enforced using a penalty method, within which the extent of contact pressure is governed by the local surface penetrations (where the default penalty stiffness parameter is automatically maximized subject to stability limits). As far as the shear stresses are concerned they are transferred via a “*slip/stick*” algorithm, that is shear stresses lower than the frictional shear stress are transferred without interface sliding (otherwise interface sliding takes place). The frictional shear stress is defined by a modified Coulomb law within which there is an upper limit to this quantity (set equal to the shear strength of the Lagrange subdomain material). The frictional shear stress is then defined as a smaller of the product between the static/kinetic friction coefficient and the contact pressure, on one hand, and the Lagrangian subdomain material shear strength, on the other. It should be recalled that the Lagrangian portion of the model is rigidized so that the shear strength is effectively made infinitely large.

In addition to the Eulerian-Lagrangian contacts, interactions (of a “*sticky*” character) also occur between different Eulerian materials. This type of interactions is a consequence of the kinematic constraint which requires that all Eulerian materials residing in a single Eulerian element are subjected to the same strain. The Eulerian-Eulerian contacts allow normal (tensile and compressive) stresses to be transferred between adjoining materials while no slip at the associated material boundaries is allowed.

Material Model(s): As mentioned earlier, the Eulerian domain was filled with air, mine and the soil. Also, the Lagrangian portion of the model is rigidized. A material model for air was presented in the previous section. The Lagrangian (rigid) material is fully defined by its density. Hence, in this section material models for the remaining two materials, mine/C4 high-energy explosive and soil, are presented.

Material models typically define the relationships between the flow variables (pressure, mass-density, energy-density, temperature, etc.) in a computational analysis. These relations typically involve: (a) an equation of state; (b) a strength equation and (c) a failure equation for each constituent material. These equations arise from the fact that, in general, the total stress tensor can be decomposed into a sum of a hydrostatic stress (pressure) tensor (which causes a change in the volume/density of the material) and a deviatoric stress tensor (which is responsible for the shape change of the material). An equation of state is then used to define the corresponding functional relationship between pressure, mass density and internal energy density (temperature). Likewise, a (constitutive material) strength relation is used to define the appropriate equivalent plastic strain, equivalent plastic strain rate, and temperature dependencies of the material's yield strength. This relation, in conjunction with the appropriate yield-criterion and flow-rule relations, is used to compute the deviatoric part of stress under elastic-plastic loading conditions. In addition, a material model generally includes a failure criterion, i.e. an equation describing the hydrostatic or deviatoric stress and/or strain condition(s) which, when attained, cause the material to fracture and lose its ability to support (abruptly in the case of brittle materials or gradually in the case of ductile materials) normal and shear stresses. Such a failure criterion, in combination with the corresponding material-property degradation and the flow-rule relations, governs the evolution of stress during failure.

Mine/C4 High-Energy Explosive: To model the hydrodynamic response of C4 high-energy (HE) explosive, both the ideal gas and the Jones-Wilkins-Lee (JWL) [10] EOS relations are used (in separate analyses). These two types of EOS are the preferred choice for the equation of state for high-energy explosives in most hydrodynamic calculations involving detonation. The results obtained for the two EOS models are found to be qualitatively and quantitatively quite similar and, hence, only the results obtained using the JWL EOS for the C4HE are presented in this section.

The JWL equation of state is defined as [10]:

$$P = A \left(1 - \frac{w}{R_1 v} \right) e^{-R_1 v} + B_1 \left(1 - \frac{w}{R_2 v} \right) e^{-R_2 v} + \frac{wE}{v} \quad (12)$$

where the constants A , R_1 , B_1 , R_2 and w for the C4 high-energy explosive are can be found in the AUTODYN materials library [10] and v is the specific volume of the material. Within a typical hydrodynamic analysis, detonation is modeled as an instantaneous process which converts unreacted explosive into gaseous detonation products and detonation of the entire high-explosive material is typically completed at the very beginning of a given simulation. Consequently, no strength and failure models are required for high-energy explosives such as C4.

Soil: Soil is a very complicated material whose properties vary greatly with the presence/absence and relative amounts of various constituent materials (sand particles, clay, silt, gravel, etc.), and particle sizes and particle size distributions of the materials. In addition, the moisture content and the extent of pre-compaction can profoundly affect soil properties. To account for all these effects, Clemson University and the Army Research Laboratory (ARL), Aberdeen, Proving Ground, MD jointly developed [11] and subsequently parameterized (using the results of a detailed investigation of dynamic response of soil at different saturation levels, as carried out by researchers at the Cavendish Laboratory, Cambridge, UK [12–13]) the new soil model [11, 14–17]. This model (used in the present work) is capable of capturing the effect of moisture on the dynamic behavior of soil and was named the CU-ARL soil model. In the remainder of this section, a brief qualitative description is provided of this material model. In addition, in Appendix A, key functional relations constituting this model are presented and explained.

For the CU-ARL soil model, a saturation-dependent porous-material/compaction equation of state is used which, as shown in our previous work [14], is a particular form of the Mie-Gruneisen equation of state [10]. Within this equation, separate pressure vs. density relations are defined for plastic compaction (which gives rise to the densification of soil) and for unloading/elastic-reloading. Within the CU-ARL soil strength model, the yield strength is assumed to be pressure-dependent and to be controlled by saturation-dependent inter-particle friction. In addition to specifying the yield-stress vs. pressure relationship, the strength model entails the knowledge of the density and saturation-dependent shear modulus. Within

the CU-ARL soil failure model, failure is assumed to occur when the negative pressure falls below a critical saturation-dependent value, i.e. a “hydro” type failure mechanism was adopted. After failure, the failed material element loses the ability to support tensile or shear loads while its ability to support compressive loads is retained.

Mine Detonation: The mine is detonated at time equal to zero, over its entire bottom face. The detonation of the remainder of the mine and the associated release of the explosive energy are then governed by the arrival of a planar detonation front, moving at a constant speed.

Computational Algorithm: The governing mass, linear momentum, energy conservation and heat conduction equations are solved within ABAQUS/Explicit with a second-order accurate, conditionally stable, explicit finite element algorithm. The same computational algorithm, as the one described and used in the previous section, was employed in this portion of the work.

Computational Accuracy, Stability and Cost: A standard mesh-sensitivity analysis was carried out (the results not shown for brevity) in order to ensure that the results obtained are accurate, i.e. insensitive to the size of the elements used.

As in the previous analysis, due to the conditionally-stable nature of the explicit finite element analysis used, the maximum time increment during each computational step had to be lower than the attendant stable time increment. A typical 10ms computational analysis followed by a detailed post-processing data-reduction analysis required on average 30 minutes of (wall-clock) time on a 12 core, 3.0GHz machine with 16 GB of memory.

IV.2 RESULTS AND DISCUSSION

Examples of typical results obtained in this portion of the work are displayed in Figures 10(a)–(b). In Figure 10(a), percent reduction (relative to the SBS case without side-channels) in the total blast momentum resulting from the use of the side-vent channels is plotted as a function of channel width, at two different exit-to-inlet cross-sectional-area ratios of the channel and a constant value (0.03m) of the charge Depth Of Burial (DOB). The results displayed in this figure show that: (a) the downward thrust

is capable of reducing the blast momentum transferred to the SBS; (b) the effect is, however, quite small (maximum around 4%); (c) the case associated with the larger area ratio yields slightly higher percent momentum reduction; (d) at each of the cross-sectional-area ratios considered, there appears to be a range of channel widths which yield maximum momentum reduction effects; and (e) at very small lower channel widths, the presence of the side-channels could be detrimental since it increases the blast momentum transferred to the SBS.

The results displayed in Figure 10(b) show the effect of channel width on the percent reduction in the total blast momentum at three different (0.03m, 0.06m and 0.09m) explosive-charge DOBs and at a constant value (1.6) of the exit-to-inlet cross-sectional-area ratio of the channel. The results presented in this figure show that the beneficial effect of the channel is still present (but, somewhat lower) in the case of larger DOBs. These results are consistent with the fact that, as the DOB increases, larger fraction of the soil is present in the fluid passing through the channel. This in turn, reduces the extent of air-based isentropic-expansion effects responsible for the observed momentum reduction.

V. THREE-DIMENSIONAL MINE-BLAST FLUID-STRUCTURE-INTERACTION ANALYSIS

In the previous section, a two-dimensional fluid-structure-interaction analysis was carried out in order to assess the potential of the side-channels in lowering the blast momentum transferred to the SBS through the downward thrust effects. The results obtained revealed the beneficial effects of the side-channels but the magnitude of these effects was quite small. Since the analysis presented in the previous section does not consider the role of all three-dimensional effects, a more complete three-dimensional analysis of the mine blast and the associated fluid structure interactions is presented in this section.

V.1 COMPUTATIONAL PROCEDURE

The computational procedure used in this portion of the work is almost identical to the one employed in the previous section. Hence, details regarding this procedure

will not be repeated here. Instead, only the aspects of the analysis which differ from their counterparts presented in the previous section will be overviewed.

Computational Domain: The computational domain used again consists of two separate subdomains, one of an Eulerian type and the other of a Lagrangian type, Figure 11. The Eulerian subdomain is again filled with sand/soil, mine/detonation products and the ambient air and is of a parallelepiped shape. This subdomain is discretized using hexahedral first-order reduced-integration Eulerian elements. It should be noted that due to the inherent symmetry of the problem, only one-quarter of the computational model is explicitly analyzed.

As far as the Lagrangian subdomain is concerned, it consists of the SBS, V-hull and side channels. The Lagrangian subdomain is meshed using quadrilateral shell elements and rigidized to form a single rigid body. During the channel-geometry optimization, the channel inlet cross-sectional area and the outlet-to-inlet area ratio are varied.

Computational Accuracy, Stability and Cost: A standard mesh-sensitivity analysis was again carried out (the results not shown for brevity) in order to ensure that the results obtained are accurate, i.e. insensitive to the size of the elements used. A typical 10 ms computational analysis followed by a detailed post-processing data-reduction analysis required on average 60 minutes of (wall-clock) time on a 12 core, 3.0 GHz machine with 16 GB of memory.

V.2 RESULTS AND DISCUSSION

In order to assess the full blast-mitigation potential of the proposed venting system, three distinct SBS configurations were examined. The main among these configurations are shown in Figures 12(a)–(c). The SBS configuration shown in Figure 12(a) has no side-vent channels. The SBS configuration shown in Figure 12(b) contains constant-radius side-vent channels. The SBS configuration shown in Figure 12(c) is very similar to that shown in Figure 12(b) except for the flaring of the side-vent channels (in their exit section). The basic configuration analyzed in the present work is that shown in Figure 12(c). A comparison of the results obtained using configurations

displayed in Figures 12(a)–(c) enable respectively assessment of the blast-mitigation effects arising from the: (i) presence; and (ii) flaring of the side-vent channels.

The computational analyses carried out in this portion of the work yielded the results pertaining to the temporal evolution and spatial distribution of various field quantities such as material-particle velocities, Euler-material volume fractions, pressure, density, etc. In addition, results pertaining to the explosive-charge detonation-induced loading experienced by, and the subsequent response of, the SBS structure (modeled as a rigid body) were obtained. In the remainder of this section, a few prototypical results are presented and discussed.

A comparison of the prototypical Eulerian-domain total-velocity results for the SBS configuration (a) without channels; (b) with constant cross-section channels; and (c) with flared channels is shown in Figures 13(a)–(c), respectively. In these figures, the outline of the SBS structure is denoted using heavy solid black lines. In the same figures, arrows are used to show the projected direction (onto the display/projection planes) of the total-velocity vector while contours are used to denote the magnitude of the total-velocity vector. Examination of the results displayed in Figures 13(a)–(c) reveals that: (a) the presence of side-vent channels helps guide the flow of the gaseous detonation products, soil-ejecta and air along the direction parallel with the side of the V-hull. Specifically, in the no side-vent channel case, Figure 13(a), there is plenty of evidence of the impact and reflection of the gaseous detonation products, soil-ejecta and air from the V-hull side. Consequently, one would expect (and the computational results confirmed) that the largest amount of momentum is transferred to the SBS, in the absence of side-vent channels; (b) flow of the Eulerian material through the side-vent channel is seen to result in an increase in the material-particle velocity, the phenomenon which is particularly pronounced in the flared section of the side-vent channels, Figure 13(c). This phenomenon, as discussed earlier in this manuscript, leads to the development of a downward thrust to the side-vent channels and, in turn, to the SBS; and (c) when analyzing the results displayed in Figures 13(a)–(c), it should be recalled that the arrows represent only the projection of the total-velocity vector onto the displayed plane while the contours pertain to the total-velocity vector overall magnitude. In other words, the fact that there are fewer and shorter arrows in Figure

13(a) relative to Figure 13(c) indicates that a substantial component of the flow takes place in a direction normal to the display plane. This observation re-emphasizes the previously made point regarding the role of side-vent channels in guiding the flow in a direction parallel with the V-hull side.

Spatial distributions of the soil-material volume fraction at four ($0\mu\text{s}$, $20\mu\text{s}$, $40\mu\text{s}$ and $60\mu\text{s}$) post-detonation times, within a vertical section passing through the axis of one of the flared side-vent channels, are shown in Figures 14(a)–(d), respectively. In these figures, the Eulerian material with a high volume fraction of soil is represented in red, while the soil-free Eulerian material is displayed in blue. Examination of the results displayed in these figures clearly confirms the previously mentioned role of the side-vent channels in guiding the detonation products, soil-ejecta and air along the V-hull side. Specifically, in Figure 14(a), a well-defined planar interface is observed between the soil and the air. In Figure 14(b), it is seen that the ejected soil has reached the side-vent channel inlet. The soil (along with the detonation products) then enters the side-vent channel, travels through it and reaches the channel exit at the post-detonation time corresponding to Figure 14(c). Subsequently, as shown in Figure 14(d), the soil which has exited the channel flows upwards (parallel with the vertical side of the SBS cabin).

Examples of the typical results obtained in this portion of the work, which relate to the assessment of the blast-mitigation potential offered by the proposed side-vent channel concept, are displayed in Figures 15(a)–(c). These results are discussed below.

In Figure 15(a), the total transferred-momentum percent reduction (relative to the SBS case without side channels) resulting from the use of side-vent channels is plotted as a function of channel inlet-area and inlet-to-outlet area ratio. The results displayed in this figure show that there is a region in the channel inlet-area/channel outlet-to-inlet area-ratio design space which is associated with reductions in the blast momentum transferred to the SBS. However, these reductions are even smaller (maximum 3.1%) than the ones found in the two-dimensional analysis (reported in Section IV). It should be noted that the SBS mass is not constant within the design space but increases both with the channel inlet area and outlet-to-inlet area ratio. In

the portion of the design space in which the transmitted impulse takes on the lowest values, the SBS mass is ca. 1.8 % larger than that of the SBS without side channels.

In Figure 15(b), the percent reduction in maximum kinetic energy acquired by the SBS (relative to the SBS case without side channels) resulting from the use of side-vent channels is plotted as a function of channel inlet-area and inlet-to-outlet area-ratio. The results displayed in this figure show that there is a region in the channel inlet-area/channel outlet-to-inlet area-ratio design space which is associated with ca. 5 % reductions in the kinetic energy acquired by the SBS. This region of the design space nearly coincides with the one identified in Figure 15(a) in which maximum reductions in the transmitted impulse were observed.

In Figure 15(c), the percent reduction in the maximum acceleration acquired by the SBS (relative to the SBS case without side channels) resulting from the use of side-vent channels is plotted as a function of channel inlet-area and inlet-to-outlet area ratio. The results displayed in this figure show that the largest reduction in the maximum SBS acceleration is obtained in the portion of the design space in which both the channel inlet-area and channel outlet-to-inlet area-ratio acquire the largest values. In this region, the SBS mass also acquires the largest values. The results displayed in Figure 15(c) are consistent with the fact that the SBS acquires a maximum acceleration during the earlier stages of the blast/SBS interaction when the downward thrust affects are minimal or not present. Under such conditions, the (rigid) SBS response to the blast is dominated by the SBS mass.

VI. SUMMARY AND CONCLUSIONS

Based on the work presented in the manuscript, the following main summary remarks and conclusions can be drawn:

1. A new blast-mitigation solution based on the use of side-vent channels/tubes attached to the V-hull is critically assessed. The solution is inspired by the principle of operation of the “*pulse-detonation*” rocket-engines.
2. The proposed solution offers, at least, the following three benefits: (a) it does not compromise the ease of movement within the cabin space; (b) it does not interfere

with the ability of the vehicle occupants to scout their surroundings; and (c) it is not expected to degrade the vehicle's structural durability/reliability.

3. A comprehensive series of transient nonlinear dynamics finite element fluid-structure-interaction analyses under supersonic flow conditions is carried out in order to assess the blast mitigation potential of the new solution.

4. The results obtained show that the side-vent channels reduce the blast momentum by creating a downward thrust. The extent of blast momentum reduction (relative to an identical structure without side-vent channels) is ~3%. The accompanying reduction in kinetic energy acquired by the SBS is ca. 5 %, while the maximum reduction in the SBS acceleration is less than 1.5 % (and is dominated by the SBS mass rather than by the geometrical details of the side-vent channels).

5. In our future work, neglected turbulence, non-Newtonian-fluid and soil-granularity effects will be investigated to obtain a more accurate assessment of the blast momentum reduction.

VII. ACKNOWLEDGEMENTS

The material presented in this paper is based on work supported by the Army Research Office (ARO) research contract entitled "*Concept Validation and Optimization for a Vent-based Mine-blast Mitigation System*", Contract Number W911NF-11-1-0518. The authors want to thank Dr. Frederick Ferguson for his continuing interest and support.

APPENDIX A: CU-ARL SOIL MATERIAL MODEL

In this section, a brief overview is provided of the key functional relations defining the CU-ARL soil material model [14–16].

Within the CU-ARL material model, soil is considered to generally have a complex structure consisting of mineral solid particles which form a skeleton. The pores between the solid particles are filled with either: (a) a low-moisture air (this type of soil is generally referred to as “*dry soil*”); (b) water containing a small fraction of air (“*saturated soil*”); or (c) with comparable amounts of water and air (“*unsaturated soil*”). The relative volume fractions of the three constituent materials in the soil (the solid mineral particles, water and air) are generally quantified by the porosity, α , and the degree of saturation (Saturation Ratio), β , which are respectively defined as:

$\alpha = 1 - \bar{\rho} = \frac{V_p}{V}$ and $\beta = \frac{V_w}{V_p}$, where V_p is the volume of void (pores), V_w is the volume of water and V is the total volume.

The three main components of the CU-ARL soil model are overviewed in the following three sub-sections.

A.1 Equation of State

For the CU-ARL soil model, a porous-material/compaction equation of state is used which is a particular form of the Mie-Gruneisen equation of state:

$$P = P_H + \Gamma \rho (E - E_H) \quad (\text{A.1})$$

in which the internal energy density dependence of the pressure is neglected. In Eq. (A.1), the following nomenclature is used: P is pressure (a sum of the pore pressure and effective stress in the soil skeleton), ρ the (current) mass density, Γ the Gruneisen gamma parameter, E the internal energy density and the subscript H is used to denote the reference shock-Hugoniot level of a given quantity.

By assuming a linear relationship between the shock speed, U_s , and the particle velocity, U_p [21], the Hugoniot pressure, P_H , is defined using the following expression for a stationary shock [10]:

$$P_H = \frac{\rho_0 C_0^2 \eta}{(1-s\eta)^2} \quad (\text{A.2})$$

where $\rho_0 = (1-\alpha_0)\rho_{ref} + \alpha_0\beta_0\rho_w$ is the initial soil material mass density, where C_0 is the y-p equal to zero intercept in the U_s vs. U_p plot, for the homogenized soil medium [12],

$$\eta = \left(1 - \frac{\rho_0 - \alpha_0\beta_0\rho_w}{\rho - \alpha_0\beta_0\rho_w}\right) = \left(1 - \frac{(1-\alpha_0)\rho_{ref}}{\rho - \alpha_0\beta_0\rho_w}\right) \text{ the compressibility ratio, } \rho_w \text{ the density of water and}$$

the parameter s represents a rate of increase of the (average) material-particle (not to be confused with soil particle) velocity, U_p , with an increase in the shock velocity, U_s and is defined by fitting U_s vs. U_p experimental data with the following linear function:

$$U_s = C_0 + sU_p \quad (\text{A.3})$$

In the CU-ARL soil-model equation of state, the aforementioned relations for ρ_0 and η are substituted in Eq. (A.3) to get:

$$P = P_H = \frac{((1-\alpha_0)\rho_{ref} + \alpha_0\beta_0\rho_w)C_0^2 \left(1 - \frac{(1-\alpha_0)\rho_{ref}}{\rho - \alpha_0\beta_0\rho_w}\right)}{\left(1 - s \left(1 - \frac{(1-\alpha_0)\rho_{ref}}{\rho - \alpha_0\beta_0\rho_w}\right)\right)^2}, \quad \rho \leq \rho_{comp} \quad (\text{A.4a})$$

and

$$P = P_H = P(\rho_{comp}) + C_0^2(\rho - \rho_{comp}), \quad \rho > \rho_{comp} \quad (\text{A.4b})$$

where $\rho_{comp} = \left(\frac{1-\alpha_0}{1-\alpha_0 + \alpha_0\beta_0}\right)\rho_{ref} + \left(\frac{\alpha_0\beta_0}{1-\alpha_0 + \alpha_0\beta_0}\right)\rho_w$ is the density of the soil at full compaction.

To account for the effect of saturation/hydration on the values of material parameters C_0 and s , the results obtained in Refs. [12,14] are fitted to a low order polynomial in which the coefficients are set to depend on the initial level of porosity and the reference density. These relations in conjunction with Eqs.(A.4a) and (A.4b) define the dependence of pressure on ρ_{ref} , α_0 , β_0 and ρ .

The P vs. ρ relation just derived is valid only during loading and only when such loading gives rise to irreversible/plastic compaction of the porous material. It should be noted that the term loading implies an event within which the pressure is increased

(and, in the case of plastic loading, a decrease in material porosity takes place). Conversely, unloading is associated with a decrease in pressure. As shown in our previous work [17], during unloading/elastic-reloading, the P vs. ρ relationship is defined as $\frac{dP}{d\rho} = C_0^2(\rho_{ref}, \alpha_0, \beta_0)$, where the $C_0(\rho_{ref}, \alpha_0, \beta_0)$ relation can be found in Ref.[14].

A.2 Strength Model

Within the dry-soil rendition of the CU-ARL soil model, material strength (a quantity which quantifies material's resistance to inelastic distortive deformation) is assumed to be pressure dependent, controlled by inter-particle friction and to be defined by the following relation:

$$\sigma_{y,dry} = \phi_{dry} P_{dry} \approx \begin{cases} 1.3732 P_{dry} & 0 < P_{dry} \leq P_{MC} \\ 1.3732 P_{MC} & P_{dry} > P_{MC} \end{cases} \quad (\text{A.5})$$

In the case of saturated soil, the CU-ARL soil model defines pressure-dependent material strength as:

$$\sigma_{y,sat} = \begin{cases} \phi_{sat} P_{sat} & 0 \leq P_{sat} \leq P_{MC} \\ \phi_{sat} P_{MC} & P_{sat} > P_{MC} \end{cases} \quad (\text{A.6})$$

where the yield-stress-to-pressure proportionality coefficient, ϕ_{sat} , is defined as:

$$\phi_{sat} = \begin{cases} \left(0.1 + 1.2732 \frac{P_{sat}}{P_{MC}} \right) & 0 \leq P_{sat} \leq P_{MC} \\ 1.3732 & P_{sat} > P_{MC} \end{cases} \quad (\text{A.7})$$

The term P_{MC} ($=1.864 \cdot 10^5$ kPa) appearing in Eqs. (A.5)–(A.7) is the Mohr-Coulomb pressure (a pressure threshold beyond which the material strength is pressure insensitive). It should be noted that none of the Eqs. (A.5)–(A.7) include the effect of strain rate on the soil material strength. This was justified in our previous work [14], where it was shown that as long as the model is used at high deformation rates (ca. $>1.0 \cdot 10^2 \text{ s}^{-1}$), the strength and failure behavior of soil can be considered rate independent.

Within the CU-ARL soil strength model, the strength vs. pressure relationship

for unsaturated soil is defined using a linear combination of the strength/pressure proportionality coefficients in dry and the saturated soils as:

$$\sigma_{y,unsat} = \begin{cases} \phi_{unsat} P_{unsat} & 0 \leq P_{unsat} \leq P_{MC} \\ \phi_{unsat} P_{MC} & P_{unsat} > P_{MC} \end{cases} \quad (\text{A.8})$$

where

$$\phi_{unsat} = (1 - \beta_o) \phi_{dry} + \beta_o \phi_{sat} \quad (\text{A.9})$$

Defined in this way, Eqs. (A.8) and (A.9) can be also used for dry soil ($\beta_o = 0.0$) and saturated soil ($\beta_o = 1.0$).

In addition to specifying the strength vs. pressure relationship, the compaction strength model entails the knowledge of the density dependent shear modulus. Since water has no ability to support shear stresses, the shear modulus, G , of unsaturated soil is dominated by the shear modulus of the solid skeleton of the soil. However, the presence of water changes the density of the soil. Therefore, the original compaction shear modulus vs. density relationship for dry soil was appropriately modified by: (a) correcting density with a $-\alpha_o \beta_o \rho_w$ term and (b) introducing a moisture-level dependent maximum shear modulus in order to obtain a (deformation-rate independent) shear modulus vs. density relationship for soil at different saturation levels. This procedure yielded the following shear modulus vs. density functional relationships:

$$G(\text{kPa}) = \begin{cases} 5.2175 \cdot 10^{-14} (\rho - \alpha_o \beta_o \rho_w)^6 & \rho(\text{kg} / \text{m}^3) < (1 - \alpha_o \beta_o) \rho_{ref} + \alpha_o \beta_o \rho_w \\ (1 - \alpha_o \beta_o) G_{Bulk} & \rho(\text{kg} / \text{m}^3) \geq (1 - \alpha_o \beta_o) \rho_{ref} + \alpha_o \beta_o \rho_w \end{cases} \quad (\text{A.10})$$

where G_{Bulk} ($=3.73470 \cdot 10^7$) denotes the shear modulus of fully compacted dry soil. Eq. (A.10) correctly accounts for the fact that, at full compaction, the soil density is equal to $(1 - \alpha_o \beta_o) \rho_{ref} + \alpha_o \beta_o \rho_w$.

It should be noted that in the strength model developed in this section, the contribution of water to the material strength was neglected. This can be justified by recognizing the fact that viscosity of water is typically around 0.001 Pa's and that even at very high deformation rates ($1.0 \cdot 10^5 \text{ s}^{-1}$), the contribution of water to the shear strength of the soil is merely around 100Pa.

A.3 Failure Model

It is well established that the presence of moisture in soil increases the soil's cohesive strength [18]. Therefore, the magnitude of the (negative) failure pressure for soil is expected to increase with the degree of saturation (β). Also, the moisture content should be substantial ($\beta > 0.7$) before its effect on the cohesive strength of soil becomes significant [18]. To account for these two observations, within the CU-ARL soil failure model [14], the following expression was proposed for the magnitude of the (negative) failure pressure in unsaturated soil; $P_{fail\ unsat}$:

$$P_{fail\ unsat} = \beta_0^5 P_{fail\ sat} \quad (\text{A.11})$$

where $P_{fail\ sat}$ (set equal to 70kPa) is the failure pressure in saturated soil [18]. The relationship given by Eq. (A.11) correctly predicts that the cohesive strength of unsaturated soil with a degree of saturation of 0.7 is around 10-15% of that in the saturated soil.

REFERENCES

1. **F. Ma, J. Y. Choi and V. Yang**, “*Propulsive Performance of Air Breathing Pulse Detonation Engines*,” **Journal of Propulsion and Power**, **22**, **6**, 2006, 1188-1203.
2. **J. Capouellez, K. Drotleff, G. Wolfe, A. Cichosz, F. Helsel, A. Mikaila, J. R. Pickens , R. W. Semelsberger, S. Kerr, E. Wettlaufer, P. Massoud, J. Wood and B. Barringer**, “*Optimized Light Tactical Vehicle*,” **27th Army Science Conference**, No. FP-11, 2010, 1-8.
3. **Z. C. Owens and R. K. Hanson**, “*Single-Cycle Unsteady Nozzle Phenomena in Pulse Detonation Engines*,” **Journal of Propulsion and Power**, **23**, 2007, 325-337.
4. **X. He and A. R. Karagozian**, “*Numerical Simulation of Pulse Detonation Engine Phenomena*,” **Journal of Scientific Computing**, **19**, 2003, 201-224.
5. **ABAQUS Version 6.10, User Documentation, Dassault Systems, 2010.**
6. **M. Grujcic, G. Arakere, H. K. Nallagatla, W. C. Bell, I. Haque**, “*Computational Investigation of Blast Survivability and Off-road Performance of an Up-armored High-Mobility Multi-purpose Wheeled Vehicle (HMMWV)*,” **Journal of Automobile Engineering**, **223**, 2009, 301-325.
7. **M. Grujcic, W. C. Bell, G. Arakere and I. Haque**, “*Finite Element Analysis of the Effect of Up-armoring on the Off-road Braking and Sharp-turn Performance of a High-Mobility Multi-purpose Wheeled Vehicle (HMMWV)*,” **Journal of Automobile Engineering**, **223**, **D11**, 2009, 1419-1434.
8. **M. Grujcic, H. Marvi, G. Arakere, W. C. Bell and I. Haque**, “*The Effect of Up-armoring the High-Mobility Multi-purpose Wheeled Vehicle (HMMWV) on the Off-road Vehicle Performance*,” **Multidiscipline Modeling in Materials and Structures**, **6**, **2**, 2010, 229-256.
9. **M. Grujcic, G. Arakere, W. C. Bell, I. Haque**, “*Computational Investigation of the Effect of Up-armoring on Occupant Injury/Fatality Reduction of a Prototypical High-mobility Multi-purpose Wheeled Vehicle Subjected to Mine-blast*,” **Journal of Automobile Engineering**, **223**, 2009, 903-920.
10. **ANSYS/AUTODYN, Theory Manual, version 6.1, 2009.**
11. **M. Grujcic, B. Pandurangan and B. Cheeseman**, “*A Computational Analysis of Detonation of Buried Mines*,” **Multidiscipline Modeling in Materials and Structures**, **2**, 2006, 363-387.
12. **A. M. Bragov, A. K. Lomunov, I. V. Sergeichev, K. Tsembelis and W. G. Proud**, “*The Determination of Physicomechanical Properties of Soft Soils from Medium to High Strain Rates*,” **International Journal of Impact Engineering**, **35**, **9**, 2008, 967-976.
13. **D. J. Chapman, K. Tsembelis and W. G. Proud**, “*The Behavior of Water Saturated Sand under Shock-loading*,” **Proceedings of the 2006 SEM Annual Conference and Exposition on Experimental and Applied Mechanics**, **2**, 2006, 834-840.
14. **M. Grujcic, B. Pandurangan, B. A. Cheeseman, W. N. Roy, R. R. Skaggs and R. Gupta**, “*Parameterization of the Porous-Material Model for Sand with Various Degrees of Water Saturation*,” **Soil Dynamics and Earthquake Engineering**, **28**, 2008, 20-35.

15. **M. Grujicic, B. Pandurangan, N. Coutris, B. A. Cheeseman, W. N. Roy and R. R. Skaggs**, “*Derivation and Validation of a Material Model for Clayey Sand for Use in Landmine Detonation Computational Analysis*”, **Multidiscipline Modeling in Materials and Structures**, **5**, **4**, **2009**, **311-344**.
16. **M. Grujicic, B. Pandurangan, N. Coutris, B. A. Cheeseman, W. N. Roy and R. R. Skaggs**, “*Computer-simulations based Development of a High Strain-rate, Large-deformation, High-pressure Material Model for STANAG 4569 Sandy Gravel*”, **Soil Dynamics and Earthquake Engineering**, **28**, **2008**, **1045–1062**.
17. **M. Grujicic, B. Pandurangan and B. Cheeseman**, “*The Effect of Degree of Saturation of Sand on Detonation Phenomena Associated with Shallow-buried and Ground-laid Mines*,” **Journal of Shock and Vibration**, **13**, **2006**, **41-62**.
18. **S. Stein and T. Kim**, “*Effect of Moisture on Attraction Force on Beach Sand*,” **Marine Geosources and Geotechnology**, **22**, **2004**, **33-47**.
19. **J. von Neumann**, “*The point source solution*,” **A. J. Taub, editor, John von Neumann: Collected Works**, **6**, **219-237**, **Pentagon Press, 1963**.
20. **S. Stein and T. Kim**, “*Effect of Moisture on Attraction Force on Beach Sand*,” **Marine Geosources and Geotechnology**, **22**, **2004**, **33-47**.
21. **G. I. Kerley**, “*The Linear U_S - u_P Relation in Shock-Wave Physics*,” **Kerley Technical Services Research Report, KTS06-1**, **2006**, **1-21**.

FIGURE CAPTIONS

Figure 1. The effect of the nozzle exit-to-throat area ratio on the exit Mach number (see text for details).

Figure 2. Pulse detonation engine with an aerodynamic valve.

Figure 3. Two blast-mitigation vehicle-hull concepts: (a) V-shaped hull; and (b) truncated V-shaped hull.

Figure 4. Side channels/tubes based blast-mitigation concept proposed in the present work.

Figure 5. A prototypical computational domain used in the transient finite element analysis of the fluid flow through the side channel.

Figure 6. Point-source solution for: (a) mass density; (b) particle velocity; (c) static pressure; and (d) temperature.

Figure 7. (a) Temporal evolution of fluid force per unit area obtained using purely Eulerian computational analysis (curve) and corresponding value (dashed line) found using the isentropic expansion analysis; (b) and (c) effectively steady axial and radial fluid velocities within the channel obtained in the same computational analysis.

Figure 8. Dependence of the impulse exerted on the fluid within the channel (solid line) on the cross-sectional area ratio. The ideal area ratio and the associated impulse per unit area (based on the time-averaged inlet pressure and the same blast-loading time) are represented by a single black-color filled square symbol.

Figure 9. A prototypical computational domain used in the two-dimensional transient finite element analysis of the mine blast detonation event: SBS-Surrogate Box Structure.

Figure 10. Two-dimensional fluid-structure interaction results pertaining to: (a) the effect of the channel width and the tube exit-to-inlet area ratio on the percent reduction in the blast momentum transferred to the SBS, at a constant depth of burial of 0.03m; and (b) the effect of the channel width and depth of burial on the same percent momentum reduction, at a constant tube exit-to-inlet area ratio of 1.6.

Figure 11. A prototypical computational domain used in the three-dimensional transient finite element analysis of the mine blast detonation event: SBS-Surrogate Box Structure.

Figure 12. Main SBS configurations analyzed in the present work: (a) the baseline v-hull configuration; (b) same as (a), but with constant-radius side vent channels; and (c) same as (b), but with channel flaring.

Figure 13. A comparison of the typical flow-field (velocity magnitude, in the present case) results for (a) the SBS configuration without channels; (b) the SBS configuration with constant cross-section channels; and (c) the SBS configuration with channel flaring.

Figure 14. Spatial distributions of the soil-material volume fraction at: (a) $0\mu\text{s}$; (b) $20\mu\text{s}$; (c) $40\mu\text{s}$ and (d) $60\mu\text{s}$ post-detonation times within a vertical section passing through the axis of one of the flared side-vent channels.

Figure 15. Percent reduction (relative to the SBS case without side-vent channels) in: (a) total blast momentum; (b) the maximum kinetic energy acquired by the SBS; and (c) the maximum SBS acceleration as a function of channel inlet-area and inlet-to-outlet area ratio.

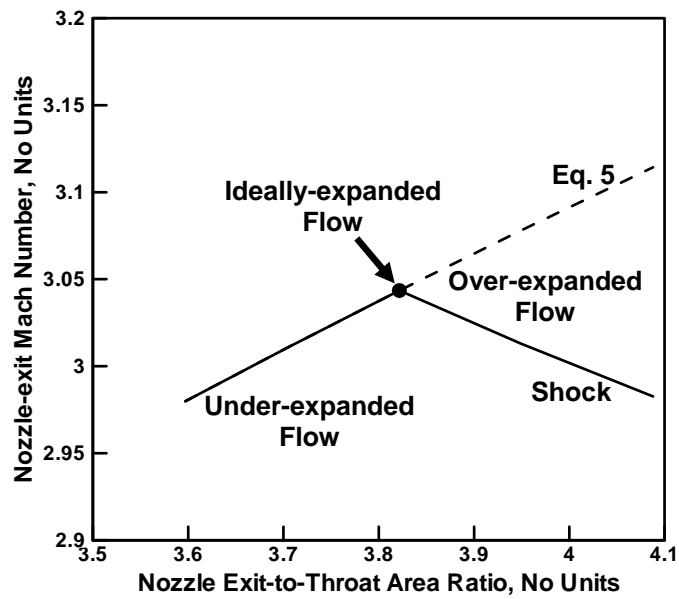


Figure 1. The effect of the nozzle exit-to-throat area ratio on the exit Mach number (see text for details).

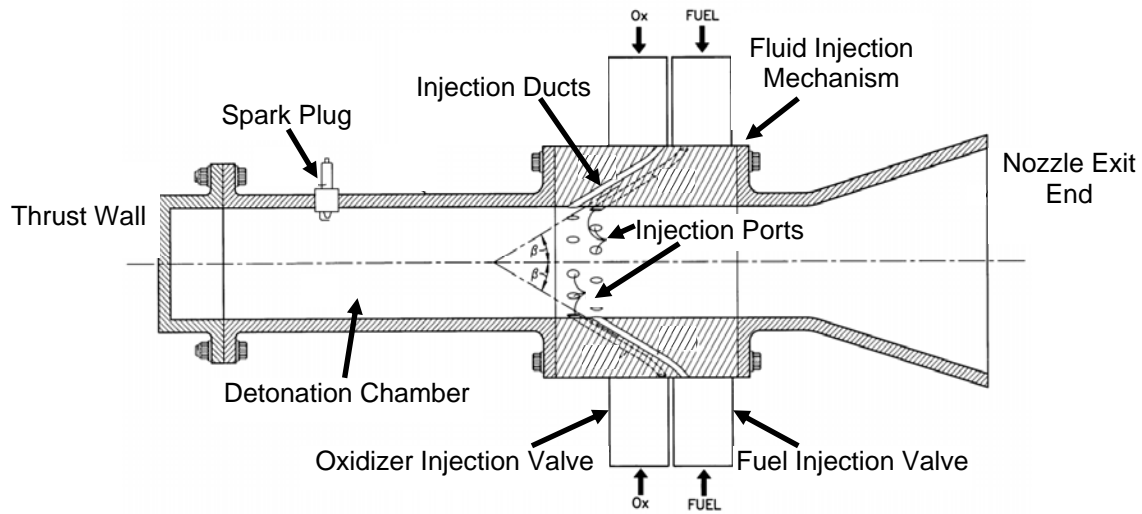


Figure 2. Pulse detonation engine with an aerodynamic valve.

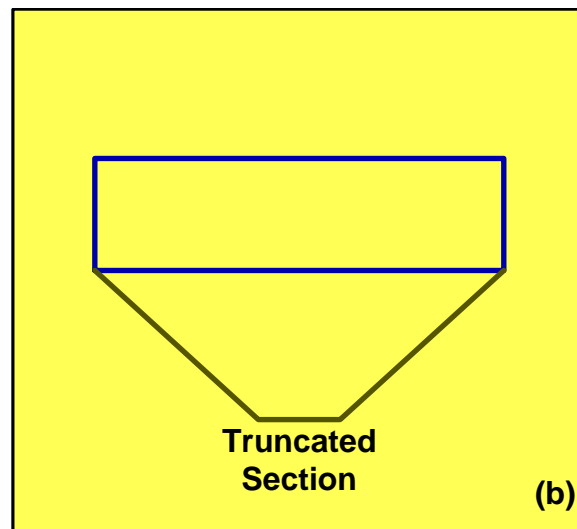
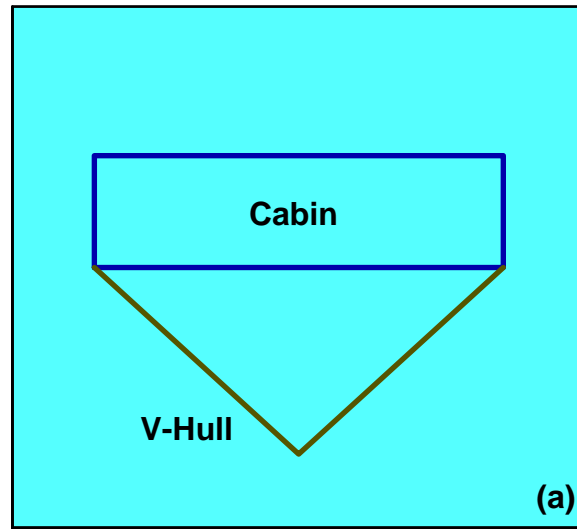


Figure 3. Two blast-mitigation vehicle-hull concepts: (a) V-shaped hull; and (b) truncated V-shaped hull.

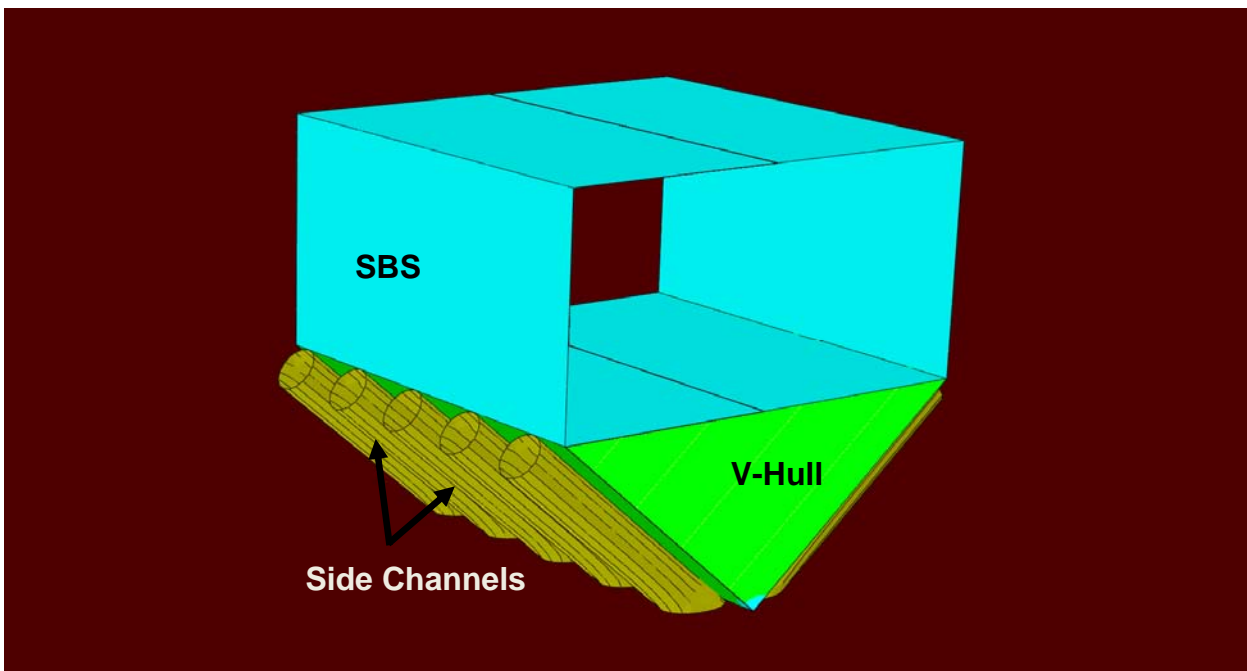


Figure 4. Side channels/tubes based blast-mitigation concept proposed in the present work.

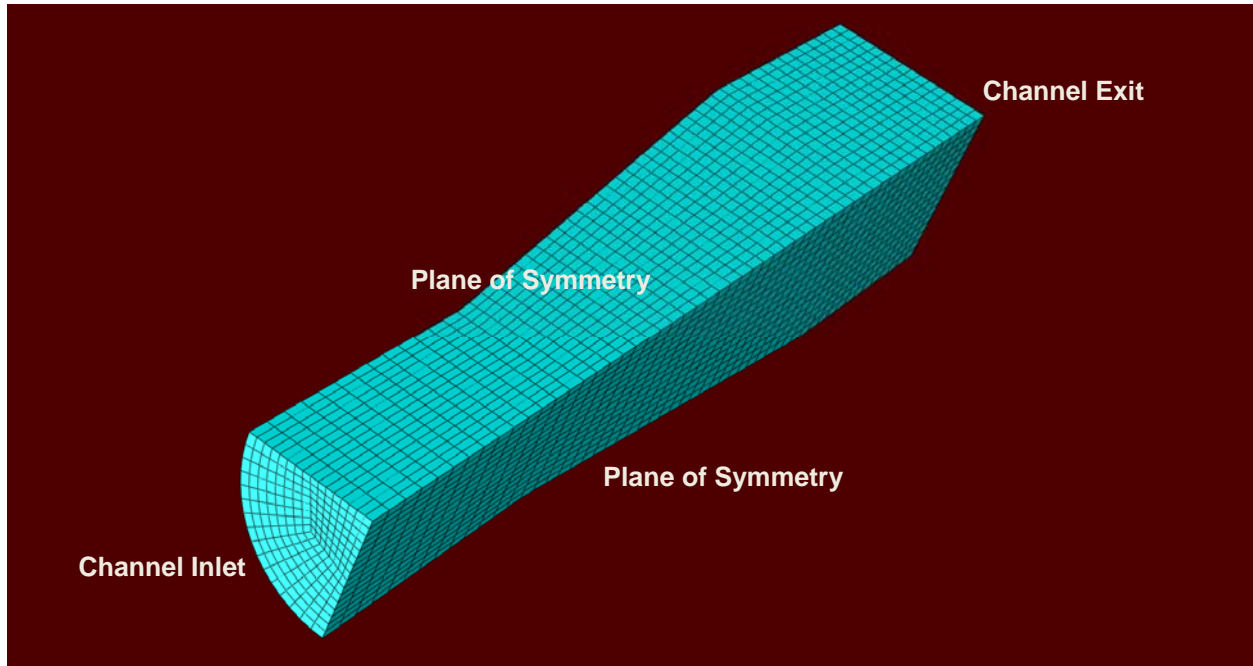


Figure 5. A prototypical computational domain used in the transient finite element analysis of the fluid flow through the side channel.

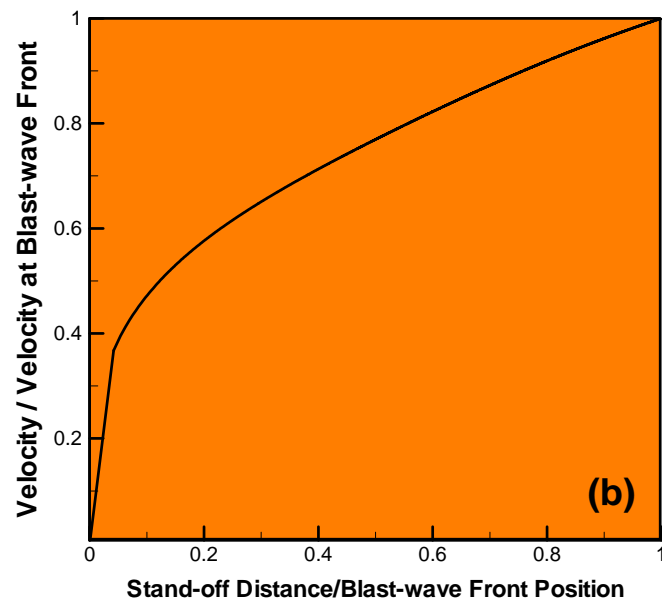
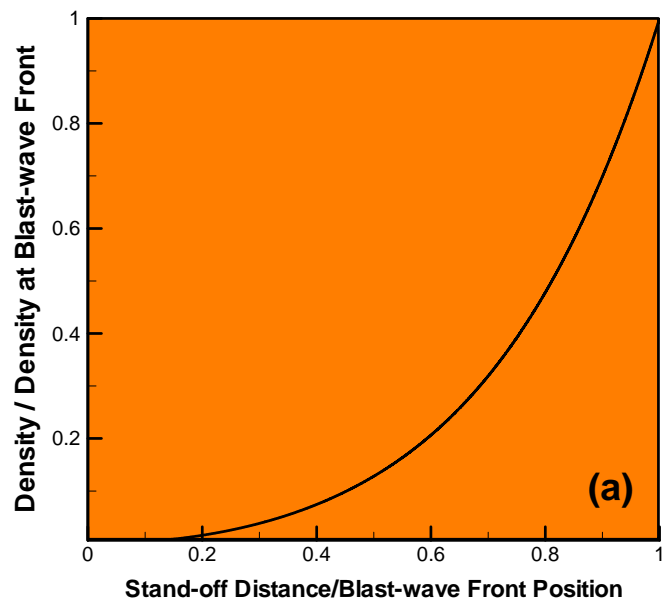


Figure 6. Point-source solution for: (a) mass density; (b) particle velocity; (c) static pressure; and (d) temperature.

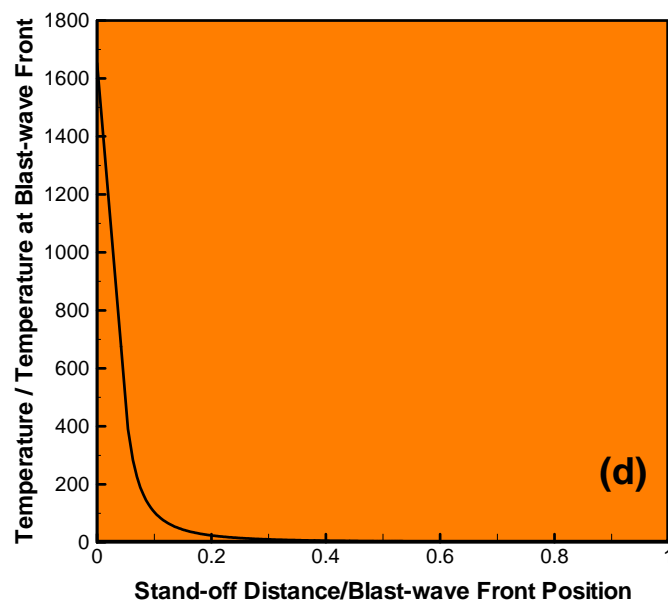
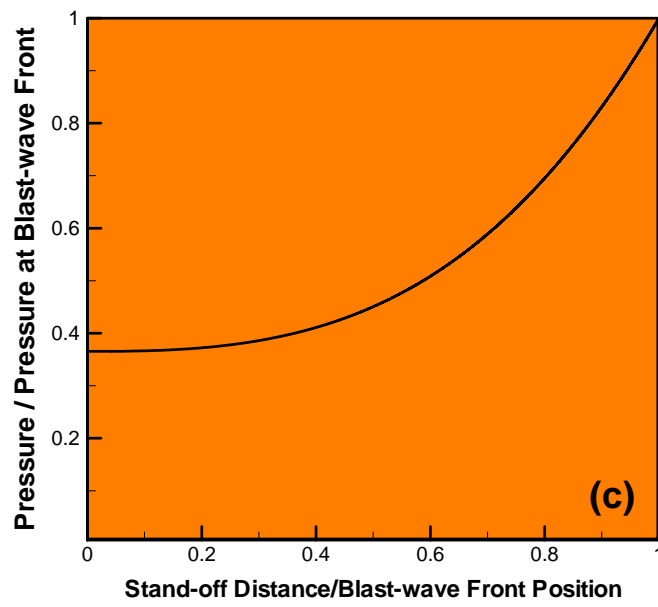


Figure 6. Continued

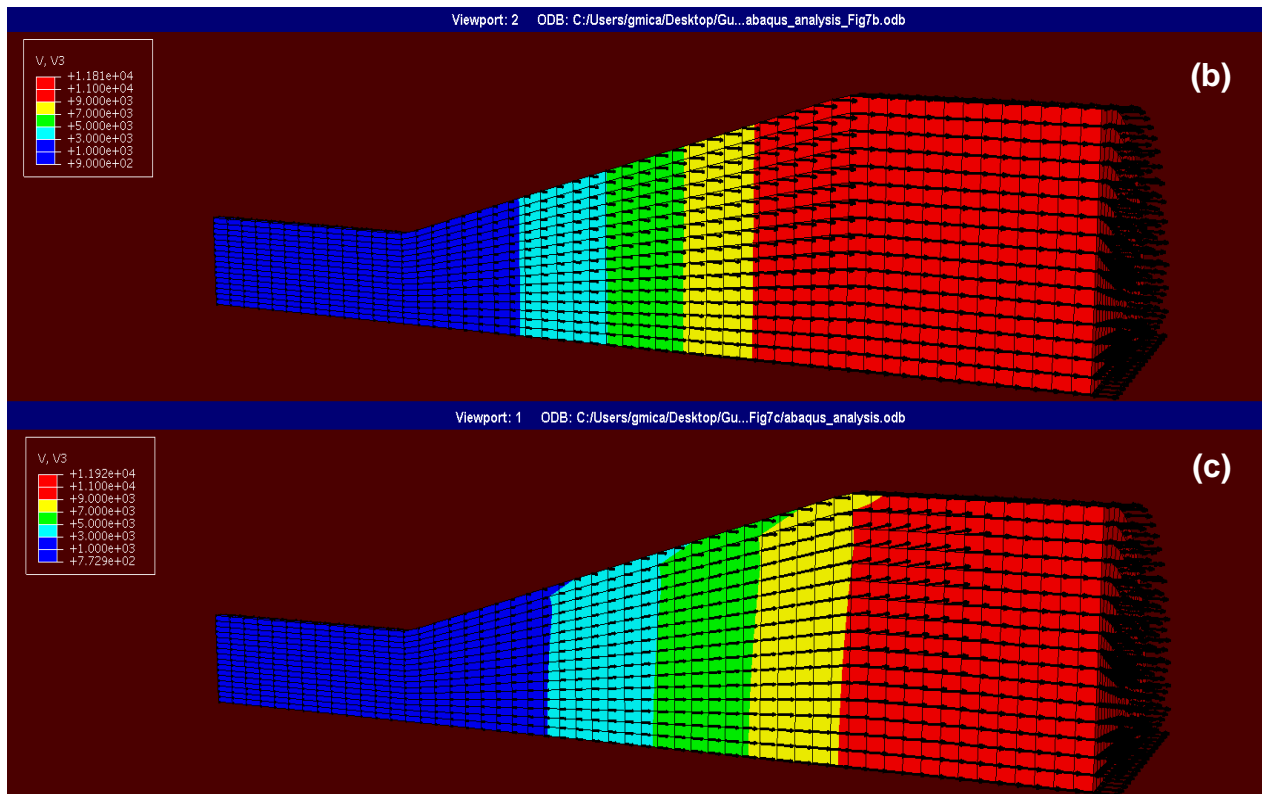
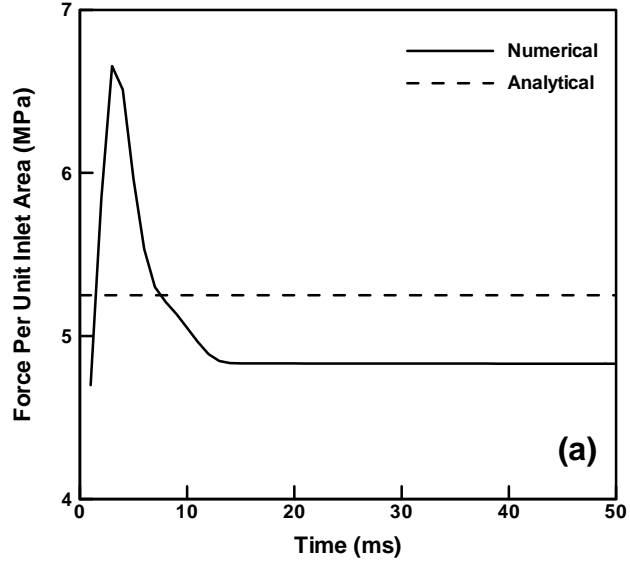


Figure 7. (a) Temporal evolution of fluid force per unit area obtained using purely Eulerian computational analysis (curve) and corresponding value (dashed line) found using the isentropic expansion analysis; (b) and (c) effectively steady axial and radial fluid velocities within the channel obtained in the same computational analysis.

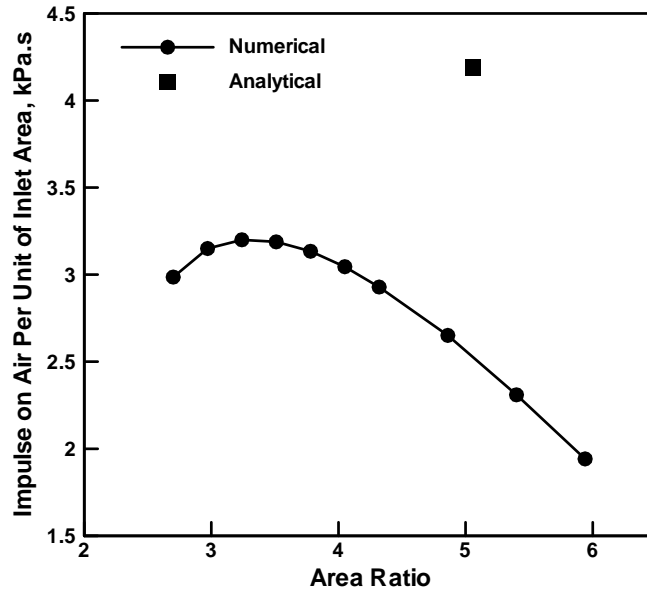


Figure 8. Dependence of the impulse exerted on the fluid within the channel (solid line) on the cross-sectional area ratio. The ideal area ratio and the associated impulse per unit area (based on the time-averaged inlet pressure and the same blast-loading time) are represented by a single black-color filled square symbol.

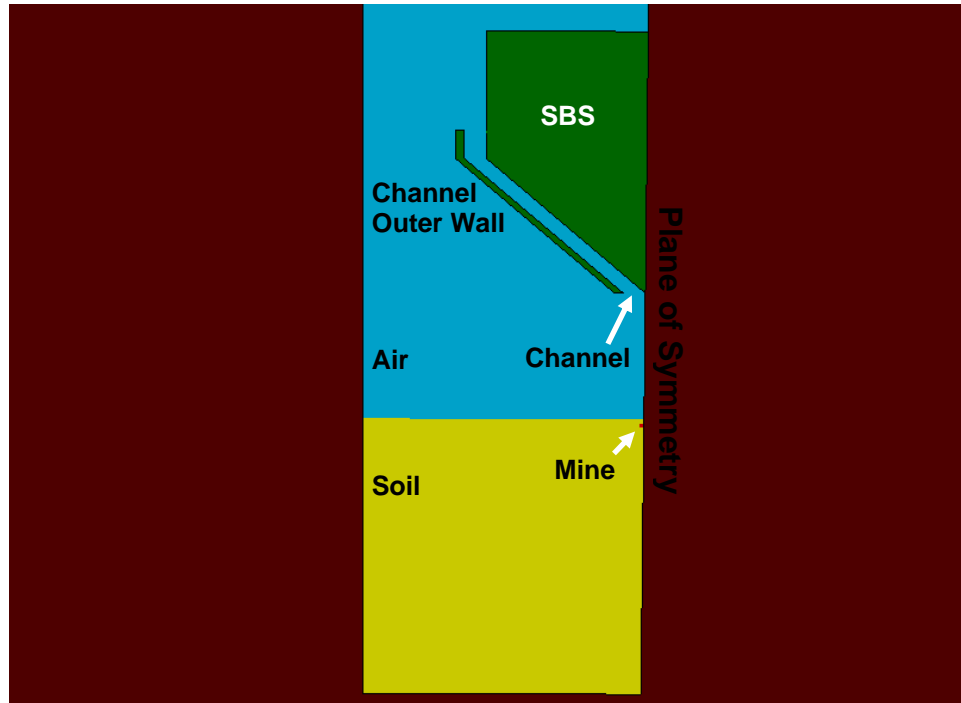


Figure 9. A prototypical computational domain used in the two-dimensional transient finite element analysis of the mine blast detonation event: SBS-Surrogate Box Structure.

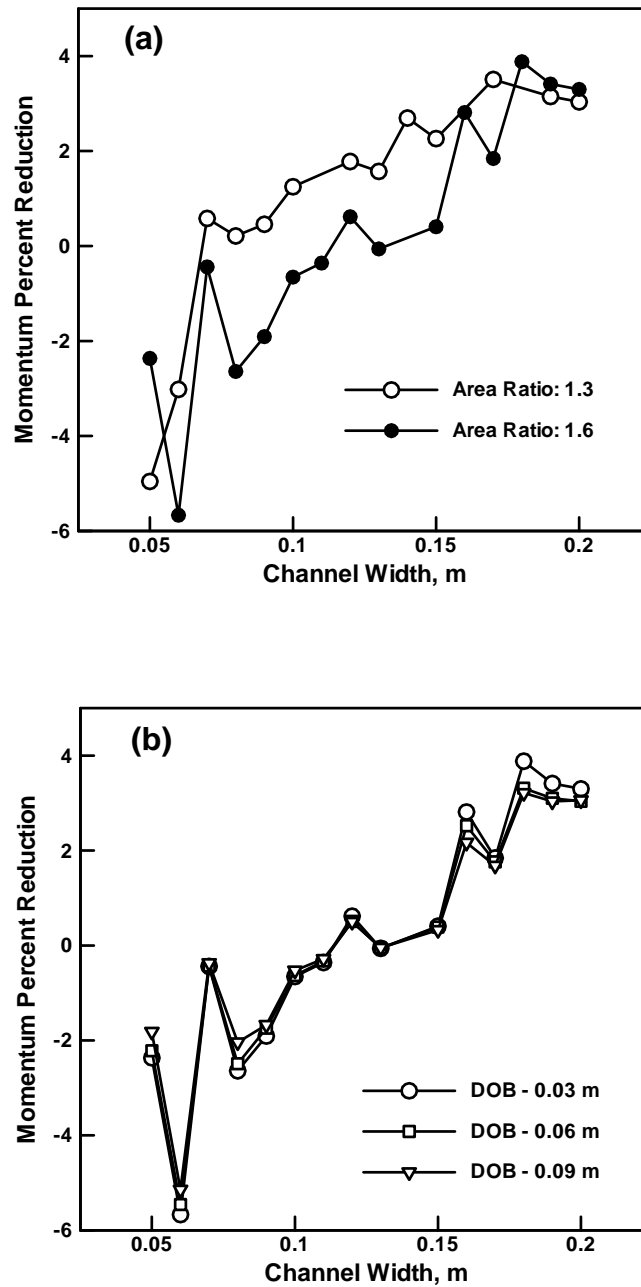


Figure 10. Two-dimensional fluid-structure interaction results pertaining to: (a) the effect of the channel width and the tube exit-to-inlet area ratio on the percent reduction in the blast momentum transferred to the SBS, at a constant depth of burial of 0.03m; and (b) the effect of the channel width and depth of burial on the same percent momentum reduction, at a constant tube exit-to-inlet area ratio of 1.6.

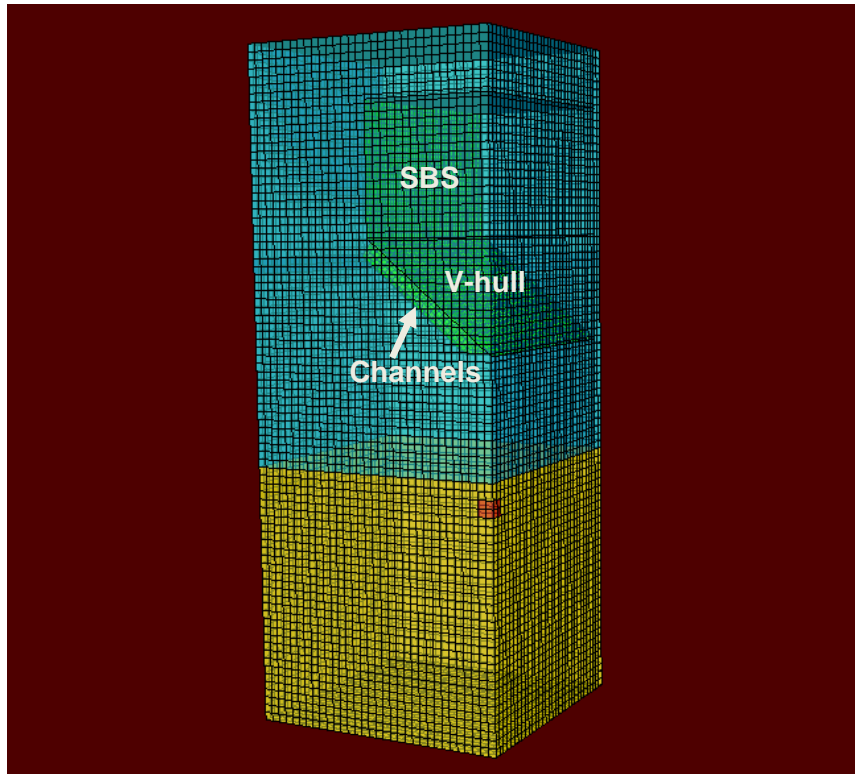


Figure 11. A prototypical computational domain used in the three-dimensional transient finite element analysis of the mine blast detonation event: SBS-Surrogate Box Structure.

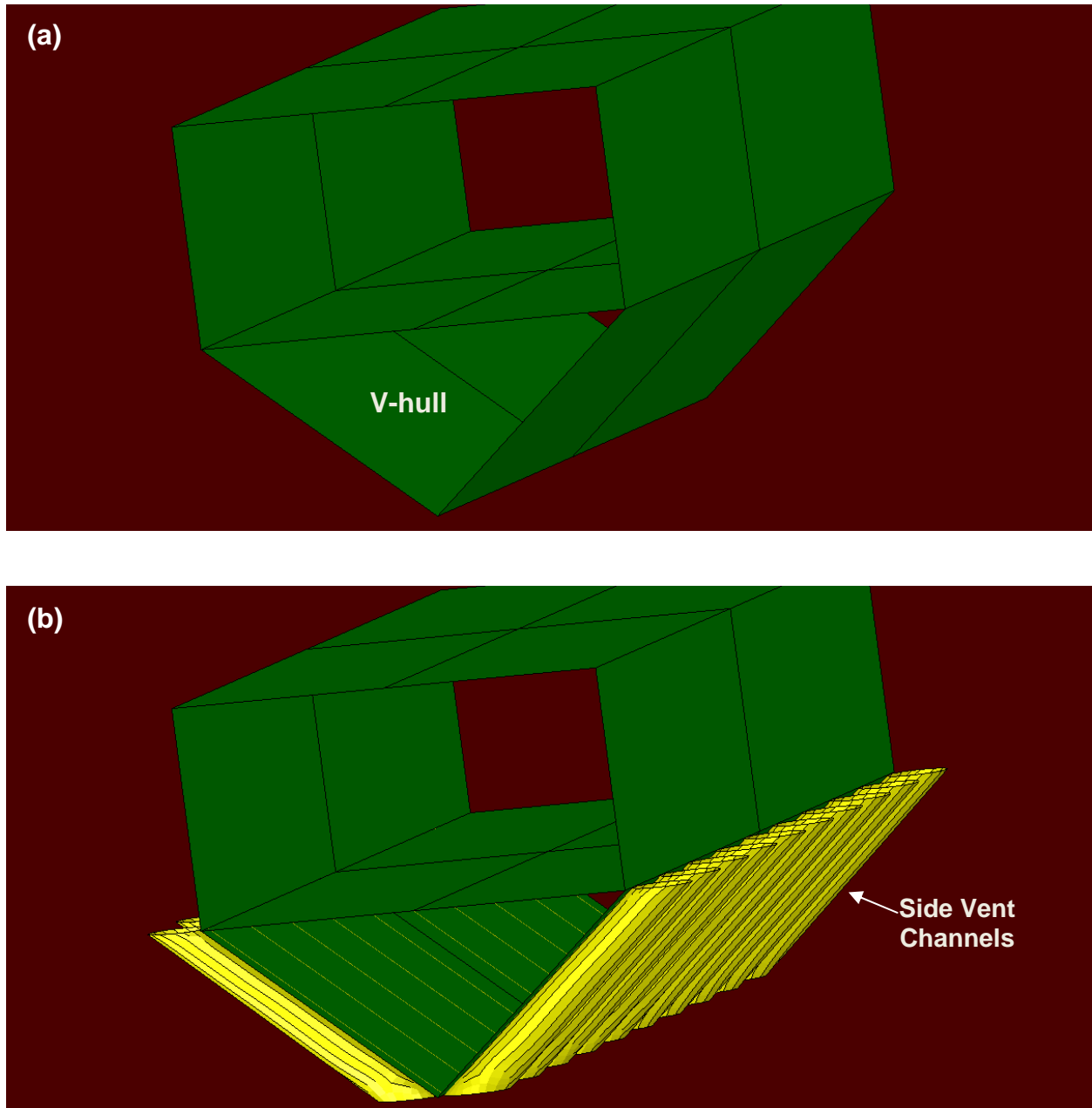


Figure 12. Main SBS configurations analyzed in the present work: (a) the baseline V-hull configuration; (b) same as (a), but with constant-radius side vent channels; and (c) same as (b), but with channel flaring.

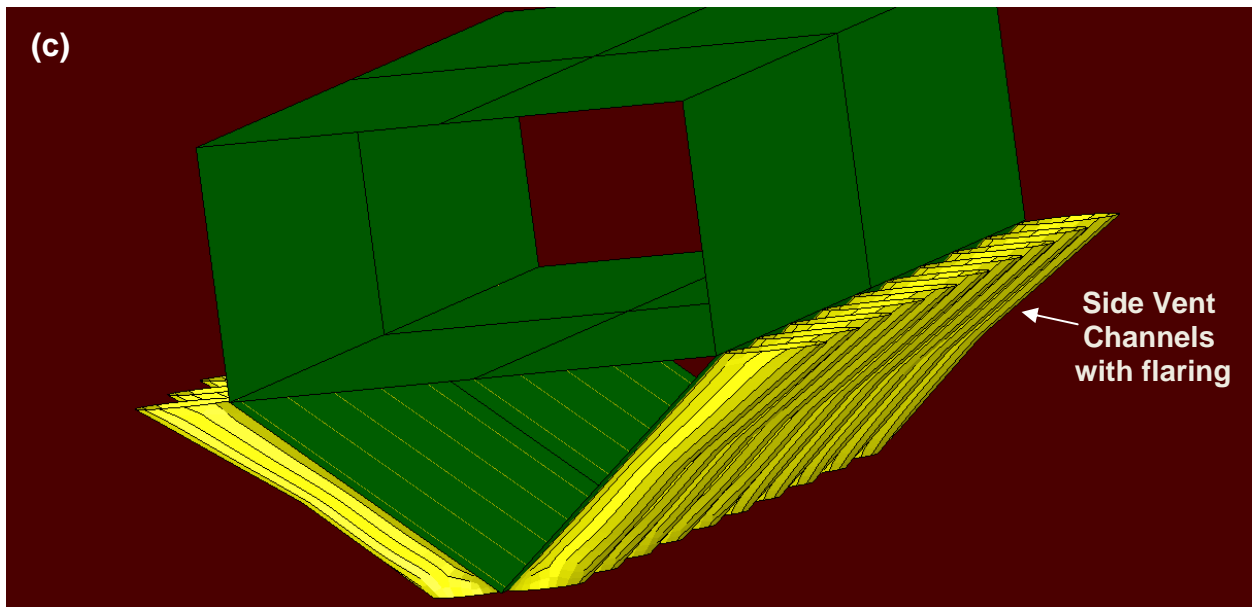


Figure 12. continued

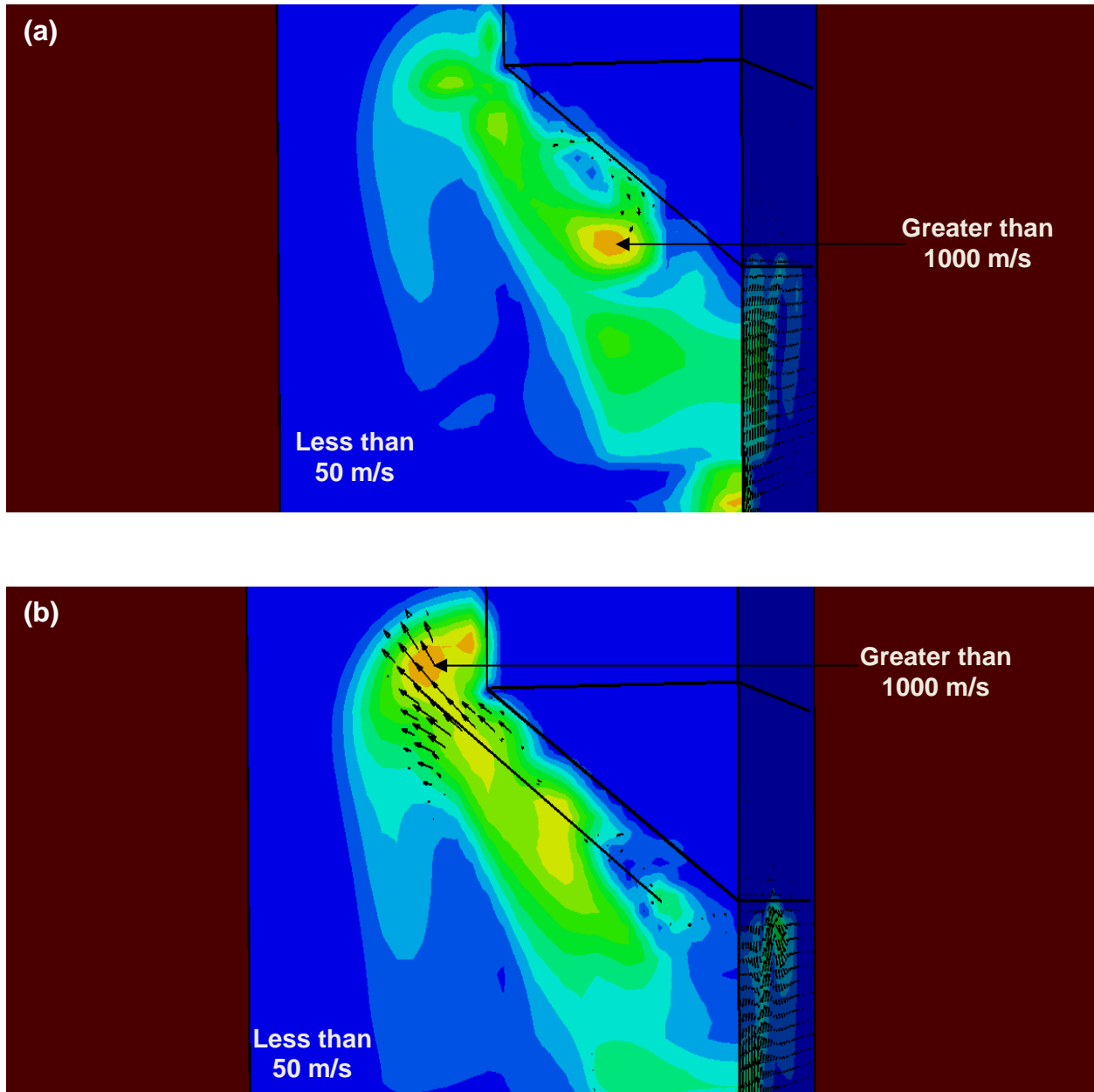


Figure 13. A comparison of the typical flow-field (velocity magnitude, in the present case) results for (a) the SBS configuration without channels; (b) the SBS configuration with constant cross-section channels; and (c) the SBS configuration with channel flaring.

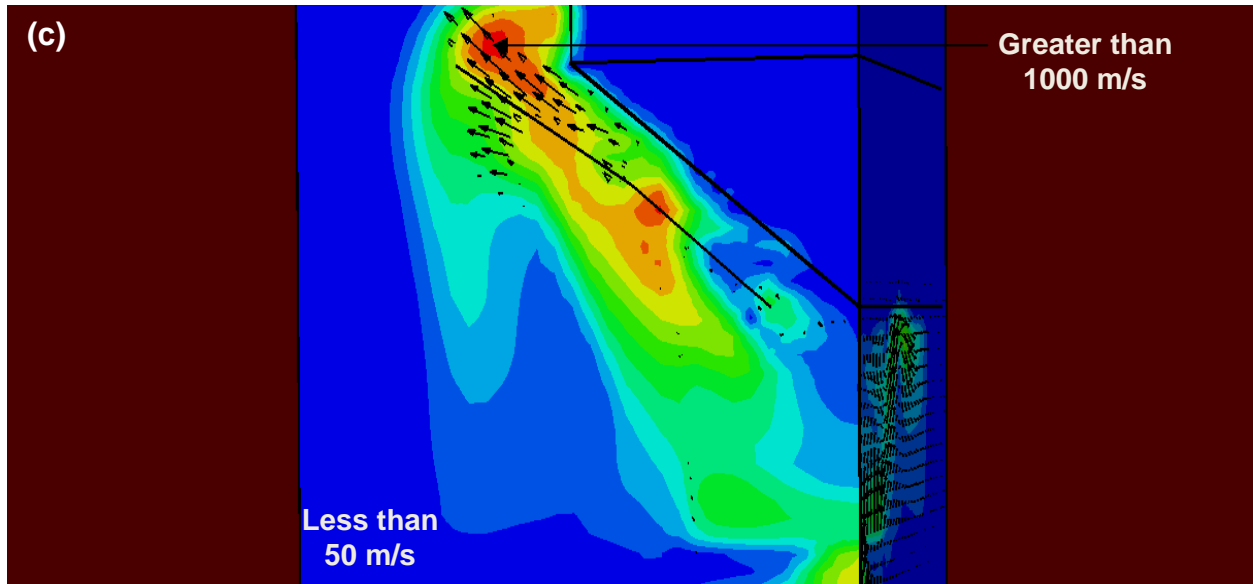


Figure 13. Continued.

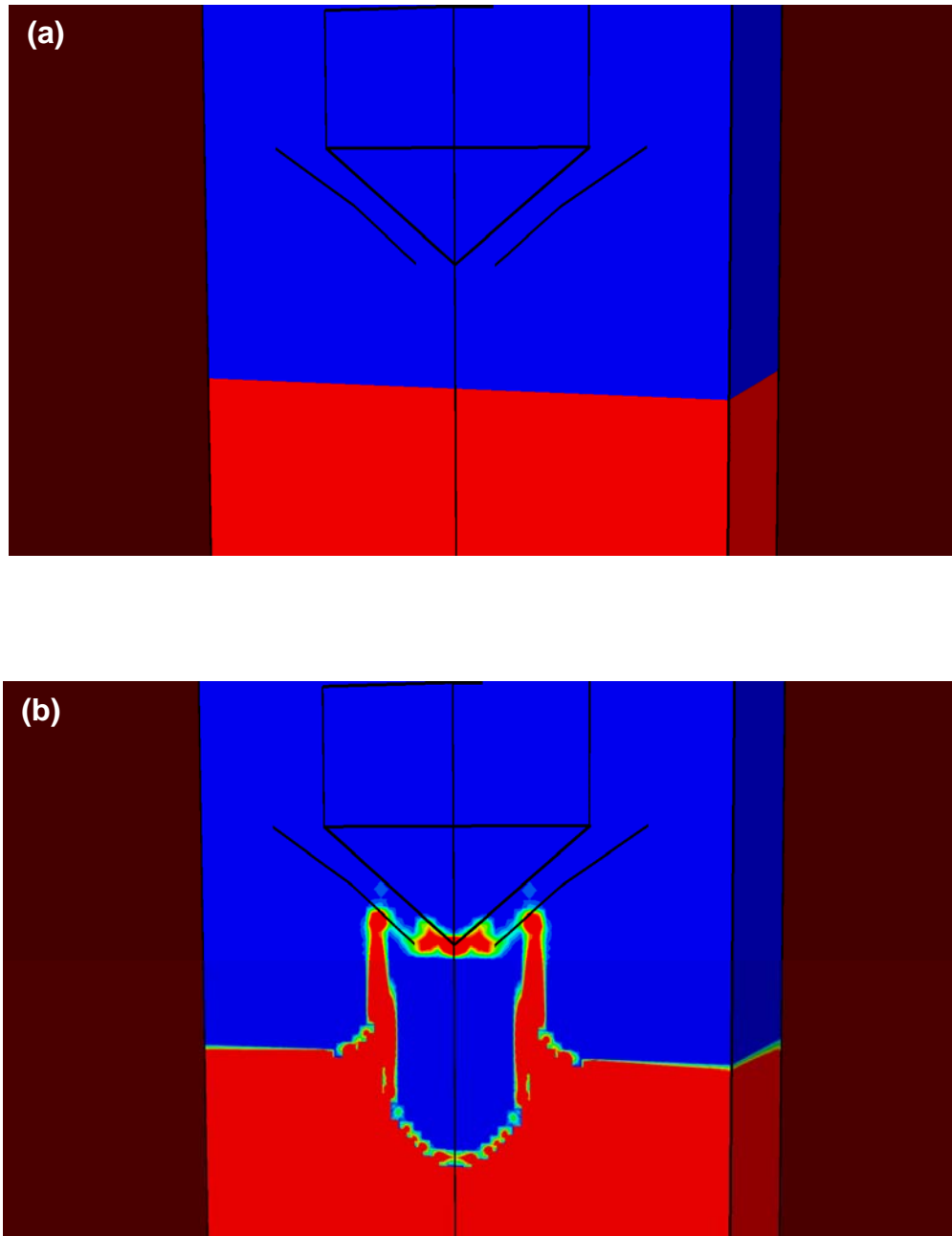


Figure 14. Spatial distributions of the soil-material volume fraction at: (a) $0\mu\text{s}$; (b) $20\mu\text{s}$; (c) $40\mu\text{s}$ and (d) $60\mu\text{s}$ post-detonation times within a vertical section passing through the axis of one of the flared side-vent channels.

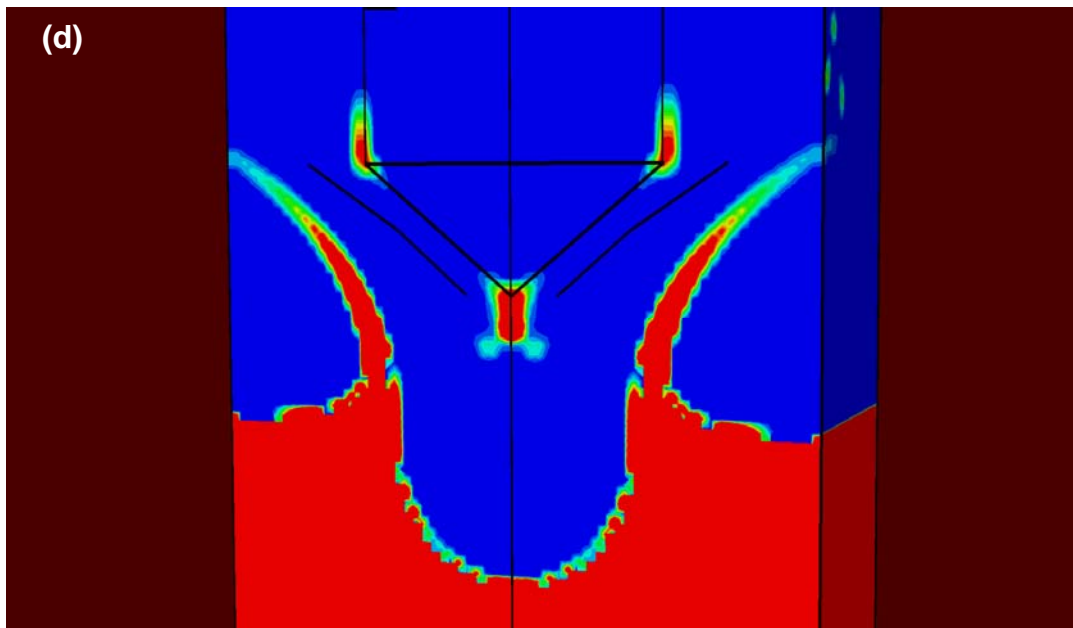
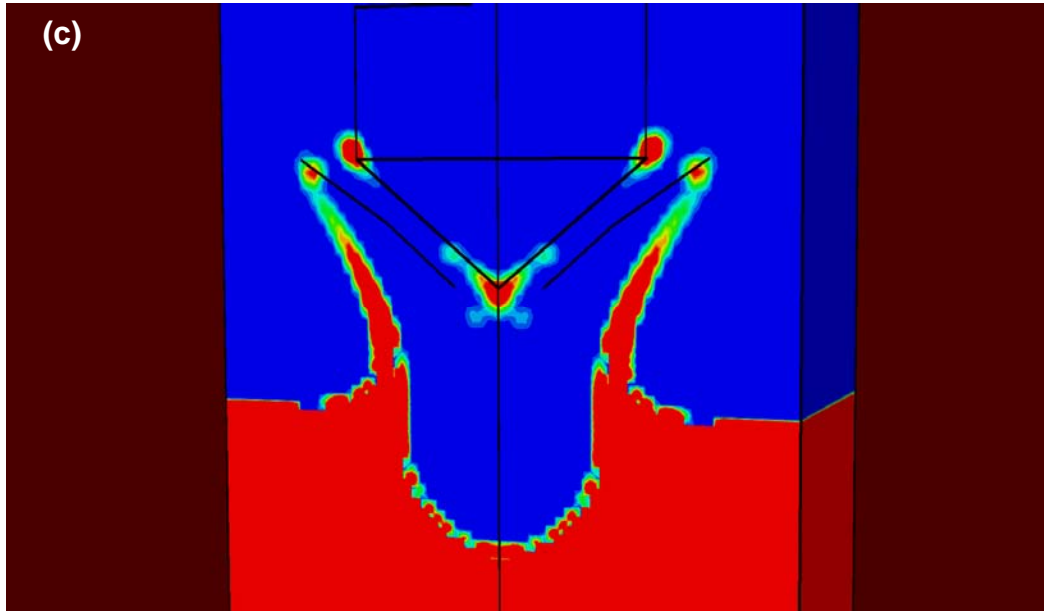


Figure 14. continued

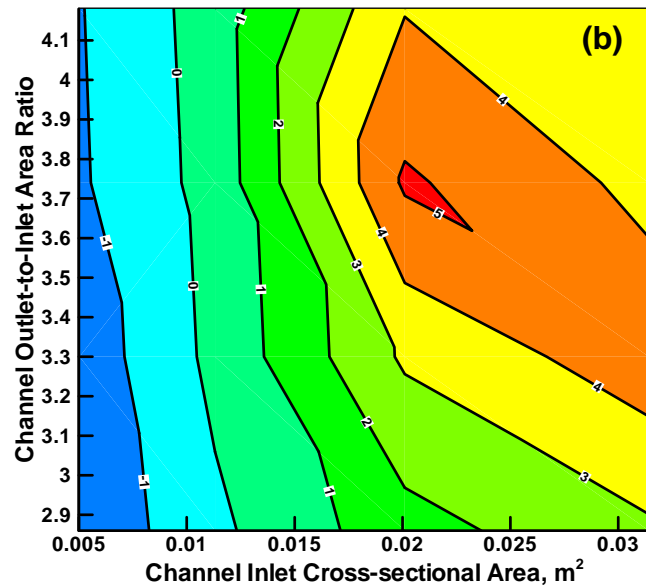
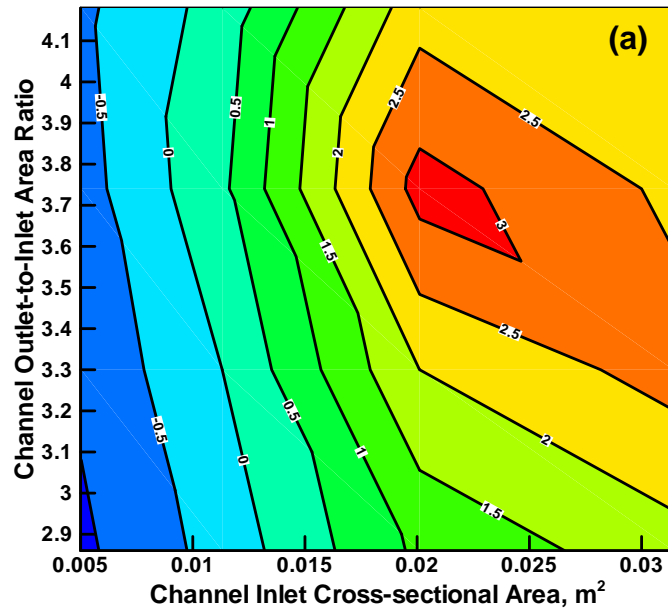


Figure 15. Percent reduction (relative to the SBS case without side-vent channels) in: (a) total blast momentum; (b) the maximum kinetic energy acquired by the SBS; and (c) the maximum SBS acceleration as a function of channel inlet-area and inlet-to-outlet area ratio.

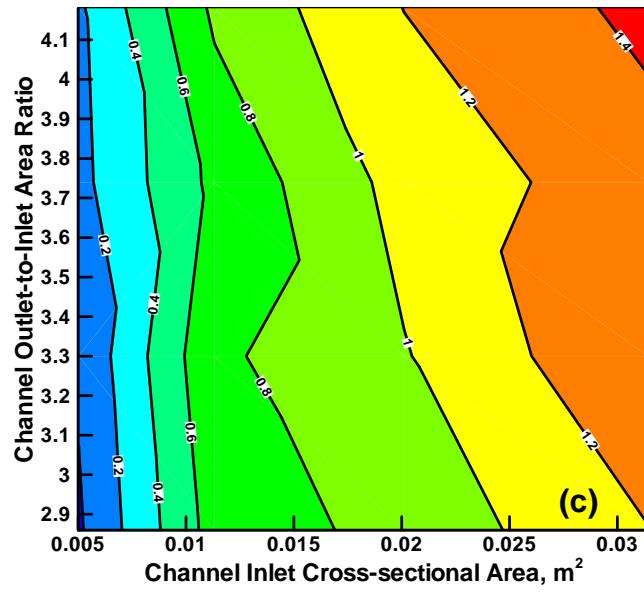


Figure 15. Continued.